JOURNAL OF GEOPHYSICAL RESEARCH, VOL. 108, NO. E12, 8064, doi:10.1029/2003JE002117, 2003

Miniature Thermal Emission Spectrometer for the Mars Exploration Rovers

Philip R. Christensen,[1] Greg L. Mehall,[1] Steven H. Silverman,[2] Saadat Anwar,[1] George Cannon,[1] Noel Gorelick,[1] Rolph Kheen,[1] Tom Tourville,[1] Duane Bates,[2] Steven Ferry,[2] Teresa Fortuna,[2] John Jeffryes,[2] William O'Donnell,[2] Richard Peralta,[2] Thomas Wolverton,[2] Diana Blaney,[3] Robert Denise,[3] Joel Rademacher,[3] Richard V. Morris,[4] and Steven Squyres[5]

Received 3 May 2003; revised 4 September 2003; accepted 11 September 2003; published 24 December 2003.

[1] The Miniature Thermal Emission Spectrometer (Mini-TES) will provide remote measurements of mineralogy and thermophysical properties of the scene surrounding the Mars Exploration Rovers and guide the rovers to key targets for detailed in situ measurements by other rover experiments. The specific scientific objectives of the Mini-TES investigation are to (1) determine the mineralogy of rocks and soils, (2) determine the thermophysical properties of selected soil patches, and (3) determine the temperature profile, dust and water-ice opacity, and water vapor abundance in the lower atmospheric boundary layer. The Mini-TES is a Fourier Transform Spectrometer covering the spectral range 5–29 μm (339.50 to 1997.06 cm^{-1}) with a spectral sample interval of 9.99 cm^{-1}. The Mini-TES telescope is a 6.35-cm-diameter Cassegrain telescope that feeds a flat-plate Michelson moving mirror mounted on a voice-coil motor assembly. A single deuterated triglycine sulfate (DTGS) uncooled pyroelectric detector with proven space heritage gives a spatial resolution of 20 mrad; an actuated field stop can reduce the field of view to 8 mrad. Mini-TES is mounted within the rover's Warm Electronics Box and views the terrain using its internal telescope looking up the hollow shaft of the Pancam Mast Assembly (PMA) to the fixed fold mirror and rotating elevation scan mirror in the PMA head located ~1.5 m above the ground. The PMA provides a full 360°of azimuth travel and views from 30° above the nominal horizon to 50° below. An interferogram is collected every two seconds and transmitted to the Rover computer, where the Fast Fourier Transform, spectral summing, lossless compression, and data formatting are performed prior to transmission to Earth. Radiometric calibration is provided by two calibration V-groove blackbody targets instrumented with platinum thermistor temperature sensors with absolute temperature calibration of ±0.1°C. One calibration target is located inside the PMA head; the second is on the Rover deck. The Mini-TES temperature is expected to vary diurnally from −10 to +30°C, with most surface composition data collected at scene temperatures >270 K. For these conditions the radiometric precision for two-spectra summing is $\pm 1.8 \times 10^{-8}$ W cm^{-2} sr^{-1}/cm^{-1} between 450 and 1500 cm^{-1}, increasing to $\sim 4.2 \times 10^{-8}$ W cm^{-2} sr^{-1}/cm^{-1} at shorter (300 cm^{-1}) and longer (1800 cm^{-1}) wave numbers. The absolute radiance error will be $< 5 \times 10^{-8}$ W cm^{-2} sr^{-1}/cm^{-1}, decreasing to $\sim 1 \times 10^{-8}$ W cm^{-2} sr^{-1}/cm^{-1} over the wave number range where the scene temperature will be determined (1200–1600 cm^{-1}). The worst-case sum of these random and systematic radiance errors corresponds to an absolute temperature error of ~0.4 K for a true surface temperature of 270 K and ~1.5 K for a surface at 180 K. The Mini-TES will be operated in a 20-mrad panorama mode and an 8-mrad targeted mode, producing two-

[1]Department of Geological Sciences, Arizona State University, Tempe, Arizona, USA.
[2]Raytheon Santa Barbara Remote Sensing, Goleta, California, USA.
[3]Jet Propulsion Laboratory, Pasadena, California, USA.
[4]NASA Johnson Space Center, Houston, Texas, USA.
[5]Department of Astronomy, Cornell University, Ithaca, New York, USA.

0148-0227/03/2003JE002117$09.00

dimensional rasters and three-dimensional hyperspectral image cubes of varying sizes. The overall Mini-TES envelope size is 23.5 × 16.3 × 15.5 cm, and the mass is 2.40 kg. The power consumption is 5.6 W average. The Mini-TES was developed by Arizona State University and Raytheon Santa Barbara Remote Sensing. *INDEX TERMS:* 5494 Planetology: Solid Surface Planets: Instruments and techniques; 5464 Planetology: Solid Surface Planets: Remote sensing; 5405 Planetology: Solid Surface Planets: Atmospheres—composition and chemistry; 5709 Planetology: Fluid Planets: Composition; 6225 Planetology: Solar System Objects: Mars; *KEYWORDS:* Mars, IR spectroscopy, mineralogy, Mars surface

Citation: Christensen, P. R., et al., Miniature Thermal Emission Spectrometer for the Mars Exploration Rovers, *J. Geophys. Res.*, *108*(E12), 8064, doi:10.1029/2003JE002117, 2003.

1. Introduction

[2] The Miniature Thermal Emission Spectrometer (Mini-TES) (Figure 1) is a Fourier transform interferometer/spectrometer intended to provide remote determination of the mineral composition of the rocks and soils, surface temperature, and atmospheric properties in the scene surrounding the Mars Exploration Rovers. The Mini-TES collects high resolution infrared spectra over the wavelengths where distinctive vibrational spectral bands are best observed, providing a direct means of identifying crystal structure, and hence mineralogy, of all geologic materials including silicates, carbonates, sulfates, phosphates, oxides, and hydroxides. The scene around the rover will be imaged by Mini-TES at two different spatial scales, creating three-dimensional hyperspectral image cubes (Figure 2). These remote mineralogic measurements, together with the morphologic and color data from the Panoramic Camera (Pancam), will be used to direct the rovers to specific targets of interest for detailed study by the full suite of rover instruments [*Squyres et al.*, 2003]. Mini-TES will also measure the temperature of the lower atmospheric boundary layer, and provide information on suspended dust, water-ice, and water vapor opacity.

[3] The Mini-TES is a miniaturized version of the Thermal Emission Spectrometer (TES) built by Arizona State University (ASU) and Raytheon Santa Barbara Remote Sensing (SBRS) for the Mars Observer (MO) and Mars Global Surveyor (MGS) missions [*Christensen et al.*, 1992]. Mars Observer was launched in 1992 and the MO TES successfully returned flight data. Unfortunately, a spacecraft anomaly occurred as the spacecraft was about to begin orbital operations in 1993. Mars Global Surveyor was launched in 1996, and the MGS TES has been returning excellent data since the spacecraft arrived at Mars in September, 1997 [*Christensen et al.*, 2001a, 2001b; *Bandfield et al.*, 2000; *Bandfield*, 2002; *Smith et al.*, 2001a, 2001b; *Kieffer et al.*, 2000; *Kieffer and Titus*, 2001].

[4] ASU and SBRS began developing an advanced and miniaturized version of the TES in 1995 under NASA Planetary Instrument Definition and Development (PIDDP) and internal SBRS funding [*Schueler et al.*, 1997]. This effort resulted in a hardware demonstration in late 1996, and in mid-1997 the Mini-TES was included as a component of the proposed Athena Precursor Experiment (APEX) for NASA's Mars 2001 Lander mission. Following the cancellation of the 2001 Lander, the Athena payload, including the Mini-TES, was selected for the Mars Exploration Rover (MER) mission.

[5] The specific scientific objectives of the Mini-TES investigation are to (1) determine the mineralogy of rocks and soils, (2) determine the thermophysical properties of selected soil patches, and (3) determine the temperature profile, dust opacity, water-ice opacity, and water vapor abundance in the lower boundary layer of atmosphere.

2. Measurement Requirements

2.1. Science Requirements

[6] The Mini-TES science objectives can be translated into a specific set of measurement requirements. Mineralogic mapping has three measurement requirements: (1) radiometric accuracy and precision necessary to uniquely determine the mineral abundances in mixtures to within 5% absolute abundance, (2) spectral resolution sufficient to uniquely determine the mineral abundances in mixtures to within 5% absolute abundance, and (3) spatial resolution of $\leq$25 cm at 10 m distance (25 mrad) necessary to resolve and identify individual rocks 0.5 m in size or larger in the rover near field. The thermophysical objective requires determining the thermal inertia to within ±10 J m^{-2} K^{-1} s$^{-1/2}$. The determination of atmospheric temperature profiles, aerosols, water vapor, and condensates has two measurement requirements: (1) radiometric accuracy and precision necessary to determine the opacities of atmospheric dust and ice to ±0.05 and temperature to ±2 K and (2) spectral resolution sufficient to uniquely identify dust, water-ice, water-vapor, and sound the atmosphere, and monitor their physical and compositional properties.

2.2. Radiometric Requirements

[7] The radiometric requirements for determining mineral abundances to 5% accuracy in mixtures depend critically on the specific minerals in question. However, in general it is necessary to resolve the relative depths of mineral absorption bands to ~2% and the absolute mineral band depths to ~10% of their typical band depth (0.15 emissivity). This produces a relative (precision) emissivity requirement, stated as the Noise Equivalent Delta Emissivity (NEDε) of 0.003 and an absolute requirement of 0.015. At typical daytime temperatures of 270 K and a reference wave number of 1000 cm^{-1} (10 μm), these requirements correspond to an absolute spectral radiance accuracy of 9 × 10^{-8} W cm^{-2} sr^{-1}/cm^{-1} and a 1-sigma (σ) radiometric precision, or noise equivalent spectral radiance (NESR), of 2 × 10^{-8} W cm^{-2} sr^{-1}/cm^{-1}. The accuracy and precision necessary to sound the atmospheric temperature profile with a <1 K temperature error and to determine the opacity of dust and ice aerosols are comparable to the mineral requirements. Determination of thermal inertia to ±10 J m^{-2} K^{-1} s$^{-1/2}$

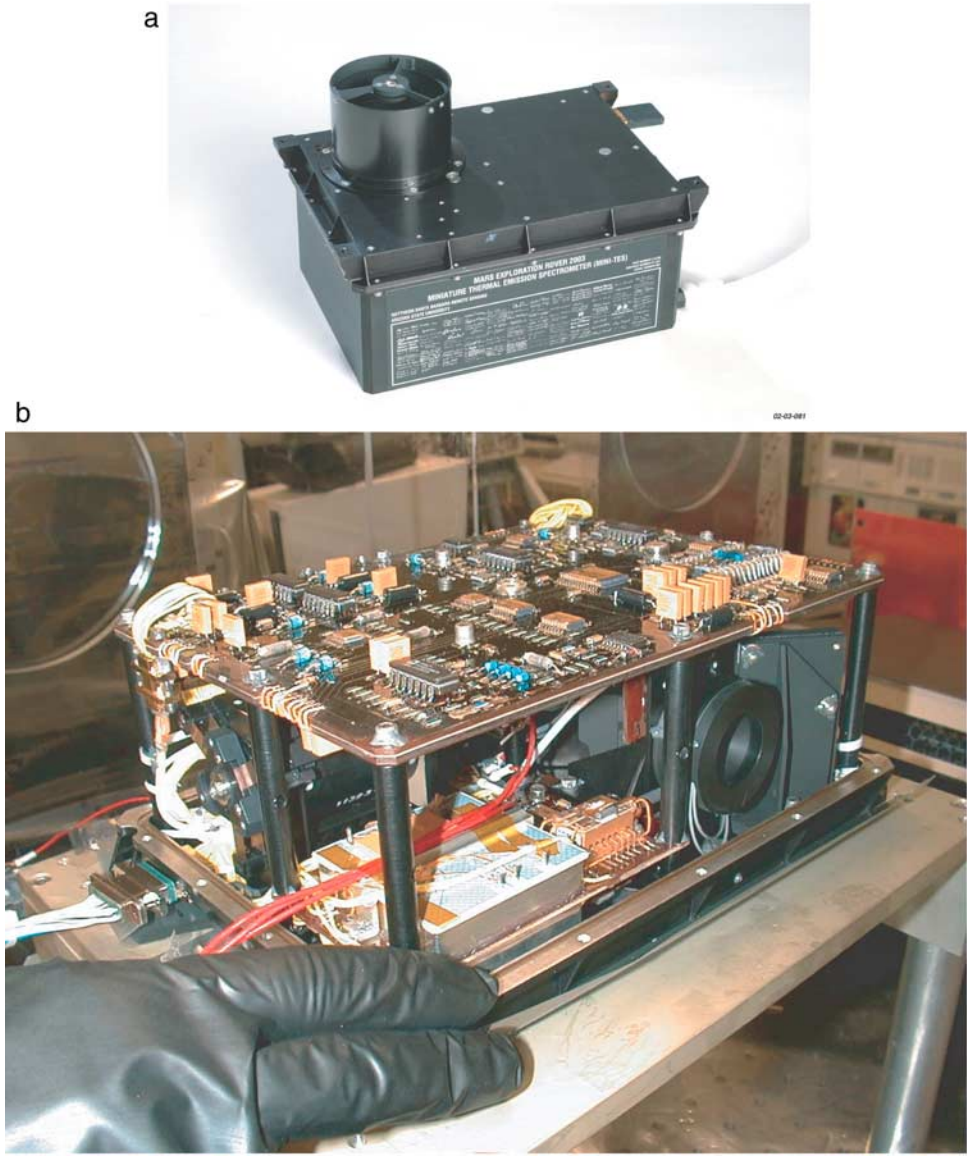

Figure 1. The Mini-TES I spectrometer following completion of testing at SBRS. (a) The instrument with its cover on and the optical aperture facing upward. (b) The Mini-TES with its protective cover off, showing the integrated packaging of the electronics and optics required to meet the size and weight constraints of the rover mission.

requires an absolute accuracy of the surface temperature determination to within ±2 K for typical night (170 K) and day (270 K) temperatures.

[8] For calibration Mini-TES views two beam-filling blackbody calibration targets whose temperatures are well known. The primary calibration target is placed within the Pancam Mast Assembly (PMA), where it can be viewed by the instrument and where it is protected from Martian dust. The secondary target is on the rover deck. Because the outer surface of the PMA is painted white and the target on the rover deck is black, the temperature difference between the targets is expected to be substantial (>20°C). The absolute accuracy of 1.5% can be achieved using internal and external calibration targets with an emissivity of >0.98, known to within ±0.005 over the Mini-TES spectra range, and absolute knowledge of the target temperature to within ±0.2°C [*Ruff et al.*, 1997].

2.3. Spectral Requirements

[9] The spectral requirements are determined by the width and position of the key spectral features in the materials and mixtures of materials. Determining mineral abundances within mixtures to 5% requires the capability to sample mineral spectral bands to ~10% of their width. For geologic materials, the full width at half maximum (FWHM) width of typical spectral bands is ~100 cm^{-1}, and the minimum in the Si-O stretching band undergoes a shift of over 150 cm^{-1} for differing crystal structures from low-to high-silica content, and an offset of up to 500 cm^{-1} from the fundamental C-O, S-O, and P-O stretching bands

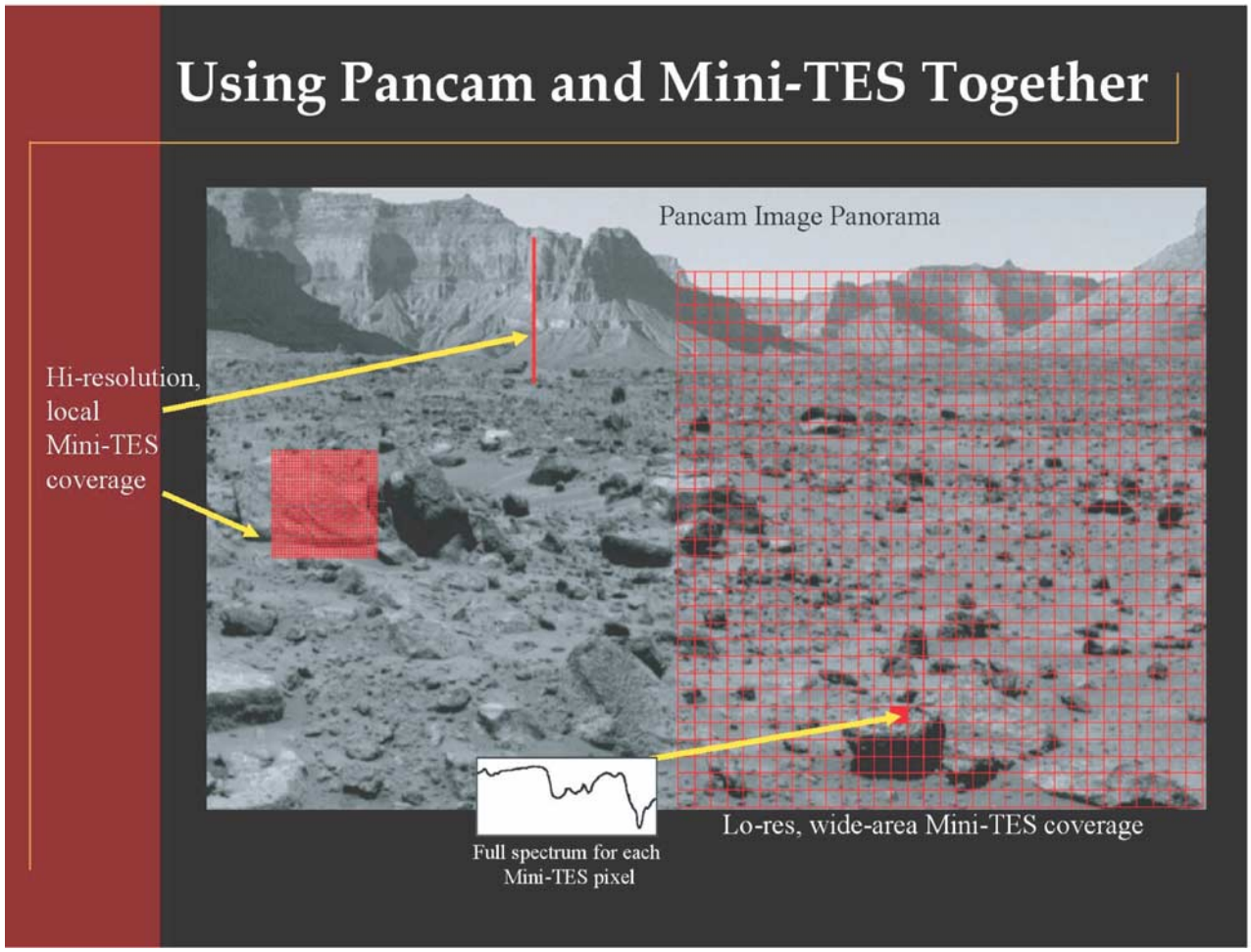

Figure 2. The size and spacing of representative Mini-TES observational grids. Both the 20-mrad (coarse) and 8-mrad grids are shown, superimposed on a simulated Pancam scene.

[*Farmer*, 1974; *Salisbury et al.*, 1992; *Christensen et al.*, 2000a]. Therefore a spectral sampling of 10 cm^{-1} is sufficient for identifying key minerals and deconvolving mineral mixtures [*Ramsey and Christensen*, 1998; *Feely and Christensen*, 1999; *Hamilton and Christensen*, 2000].

2.4. Field of View and Pointing Requirements

[10] Mini-TES views the terrain around the rover using its internal telescope looking up the hollow shaft of the PMA to a fixed fold mirror and a rotating elevation scan mirror located in the PMA head. The PMA provides a full 360°of azimuth travel, but limitations on the size of opening in the mirror assembly atop the PMA restrict the total elevation range to 80°. The mirrors were oriented to provide a 30° elevation view above the nominal horizon, allowing observation of the sky, and 50° below the nominal horizon, allowing the terrain with ~2 m of the rover to be observed. The PMA's mirror assembly is located ~1.5 m above the ground. The offsets between the Mini-TES and the Pancam were measured pre-flight to within 2 mrad, allowing data from these two instruments to be co-registered to within a single Mini-TES pixel.

[11] The Mini-TES integration time required to achieve a given signal-to-noise ratio (SNR) is inversely proportional to the fourth power of the angular resolution. This strong dependence drove the selection of two spatial resolution modes: a 20-mrad (full width half maximum (FWHM)) mode for rapid surveys of large areas, and an 8-mrad mode for detailed study of limited high-priority regions. The Mini-TES telescope aperture size results from a trade between the integration time required to obtain an adequate SNR (large telescope), and the mass of the PMA and the shadowing of the rover's solar array (small telescope). A telescope aperture of 6.35 cm (2.42 inches) was selected, resulting in a PMA that is manageable and achieves the required SNR under all daytime conditions in the 20-mrad mode by co-adding two spectra. The required SNR can be obtained with just one spectrum for the warmest mid-day conditions.

[12] The key Mini-TES requirements, along with the values achieved in the flight instruments, are summarized in Table 1.

3. Vibrational Spectroscopy

3.1. Overview

[13] Vibrational spectroscopy is based on the principle that vibrational motions occur within a crystal lattice at frequencies that are directly related to crystal structure and elemental composition (i.e., mineralogy) [e.g., *Wilson et al.*,

Table 1. Mini-TES Performance Requirements and Actual Performance

Parameter	Requirement	Actual
	Mineral Determination	
Precision (NEDε)	±0.003	±0.003
Absolute Accuracy (NEDε)	0.015	0.004 to 0.008
Radiometric Precision (NESR)	$\pm 2 \times 10^{-8}$ W cm^{-2} sr^{-1}/cm^{-1}	$\pm 1.8 \times 10^{-8}$ W cm^{-2} sr^{-1}/cm^{-1} between 450 and 1500 cm^{-1}; instrument temperature 10 to 30°C
Radiometric Accuracy	9×10^{-8} W cm^{-2} sr^{-1}/cm^{-1}	5×10^{-8} W cm^{-2} sr^{-1}/cm^{-1}
Spectral Sampling	10 cm^{-1}	9.99 cm^{-1}
Field of View	Azimuth: 0–360° Elevation: −50 to +5° from horizon	0–360° −50 to +30°
Spatial Resolution	25 mrad	17.5 and 6.9 mrad FWHM
	Atmosphere Studies	
Radiometric Precision (NESR)	$\pm 2 \times 10^{-8}$ W cm^{-2} sr^{-1}/cm^{-1}	$\pm 1.8 \times 10^{-8}$ W cm^{-2} sr^{-1}/cm^{-1} between 450 and 1500 cm^{-1}; instrument temperature 10 to 30°C
Radiometric Accuracy	9×10^{-8} W cm^{-2} sr^{-1}/cm^{-1}	5×10^{-8} W cm^{-2} sr^{-1}/cm^{-1}
Spectral Sampling	10 cm^{-1}	9.99 cm^{-1}
Field of View	Azimuth: 0–360° Elevation: −5 to +30° from horizon	0–360° −50 to +30°
Spatial Resolution	40 mrad	17.5 and 6.9 mrad FWHM
	Thermophysical Properties	
Temperature	2 K absolute	0.4 (day) to 1.5 K (night)

1955; *Farmer*, 1974]. The fundamental frequencies of geologic materials typically correspond to wavelengths greater than ~5 μm, and provide a diagnostic tool for identifying virtually all minerals.

[14] An extensive suite of studies over the past 40 years has demonstrated the utility of vibrational spectroscopy for the quantitative determination of mineralogy and petrology [e.g., *Lyon*, 1962; *Lazerev*, 1972; *Vincent and Thompson*, 1972; *Farmer*, 1974; *Hunt and Salisbury*, 1976; *Salisbury et al.*, 1987a, 1987b; *Salisbury and Walter*, 1989; *Bartholomew et al.*, 1989; *Salisbury et al.*, 1991; *Salisbury*, 1993; *Christensen and Harrison*, 1993; *Lane and Christensen*, 1997, 1998; *Feely and Christensen*, 1999; *Christensen et al.*, 2000a; *Hamilton*, 2000; *Hamilton and Christensen*, 2000; *Wyatt et al.*, 2001; *Hamilton et al.*, 2001]. The fundamental vibrations within different anion groups, such as CO_3, SO_4, PO_4, and SiO_4, produce unique, well separated spectral bands that allow carbonates, sulfates, phosphates, silicates, and hydroxides to be identified (Figure 3). Additional stretching and bending modes involving major cations, such as Mg, Fe, Ca, and Na, allow identification of specific minerals within the broad mineral groups. Significant progress also has been made in the development of quantitative models to predict and interpret the vibrational spectra produced by emission of energy from complex, natural surfaces [e.g., *Conel*, 1969; *Henderson et al.*, 1992; *Hapke*, 1993; *Salisbury et al.*, 1994; *Moersch and Christensen*, 1995; *Wald and Salisbury*, 1995; *Mustard and Hays*, 1997].

3.2. Mineral Groups

[15] The primary silicate minerals associated with igneous rocks are the most abundant mineral class found on Mars [*Christensen et al.*, 2000b; *Bandfield et al.*, 2000; *Christensen et al.*, 2001a; *Bandfield*, 2002], and the ability to distinguish and quantify volcanic minerals, such as feldspars, pyroxenes, and olivines, is crucial to describing the fundamental geological character of the MER landing sites. All silicates have Si-O stretching modes between 8 and

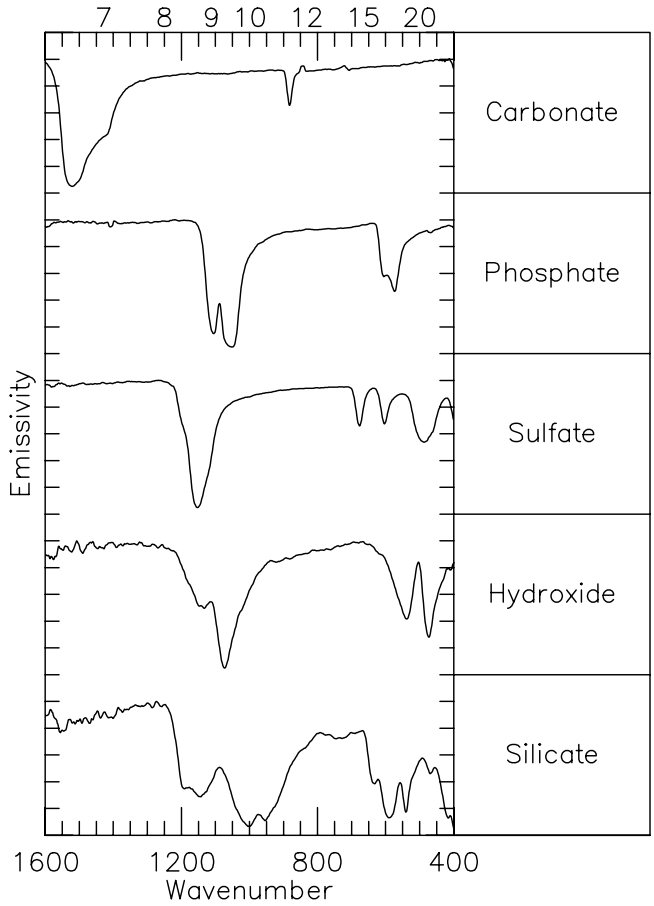

Figure 3. Thermal infrared spectra of representative mineral groups. Note the significant offset between the fundamental absorptions of the major mineral groups.

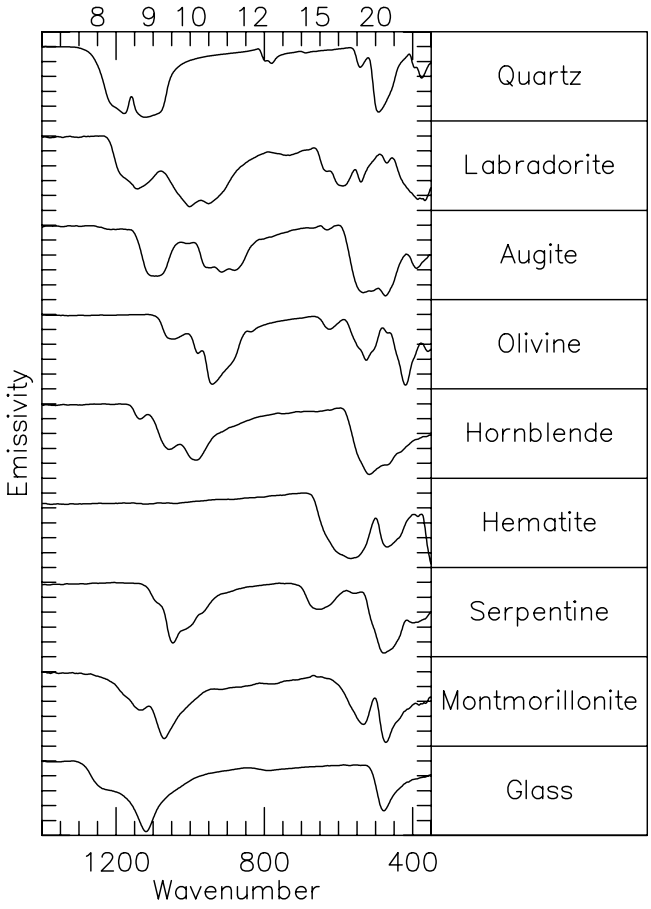

Figure 4. Examples of individual minerals within the silicate mineral group, illustrating the unique nature of these minerals over the mid-infrared spectral range. The individual spectra have been scaled and offset for clarity. These spectra are representative of the spectral sampling and radiometric precision that will be obtained from the Mini-TES. The emissivity minima in the absorption bands in these minerals vary from 0.5 to 0.8.

12 μm that vary in position with mineral structure (e.g., Figure 4). This absorption shifts to higher frequency (shorter wavelength) as bond strength increases for isolated, chain, sheet, and framework tetrahedron structure. These shifts allow for detailed identification of the igneous silicates, including variations within solid solution series.

[16] Oxides, in particular gray crystalline hematite, have been found to be an important minor component on Mars [*Christensen et al.*, 2000c; *Christensen et al.*, 2001b; *Bell and Morris*, 1999], and provided a major impetus for the selection of the Meridiani Planum landing site for the MER-B rover. The crystalline hematite at Meridiani has been suggested to form by aqueous processes [*Christensen et al.*, 2001b; *Hynek et al.*, 2002], with possible pathways from goethite, magnetite, or other iron-rich precursors [*Glotch et al.*, 2003]. The search for associated oxides or other precursor minerals will provide significant clues to the origin and history of Meridiani Planum.

[17] The evaporite mineral group includes carbonates, sulfates, chlorides, and phosphates that are precipitated from marine or non-marine waters. As such, they provide direct mineralogical evidence for standing water. The abundance of these minerals in a sedimentary basin is a function of the dissolved chemical constituents contained in the water, as well as the history of the basin inundation/denudation, and the identification and quantification of the different evaporite minerals can yield information about the environments in which they were produced. Thermal-infrared spectra provide distinguishing characteristics for the different groups, with carbonates, sulfates (gypsum) and phosphates (apatite) having deep, well-defined features in the 8.3 to 10 μm region that vary with position on the basis of composition [*Lane and Christensen*, 1998; *Farmer*, 1974].

[18] Hydrothermal systems produce characteristic mineralization that is dominated by microcrystalline quartz (chert, chalcedony, opal, etc.) and carbonates. Carbonates can precipitate in thermal spring environments, and provide evidence for wetting episodes in several Martian meteorites [e.g., *McSween*, 1994]. The fundamental C-O absorption occurs near 6.7 μm [e.g., *Farmer*, 1974; *Nash and Salisbury*, 1991; *Lane and Christensen*, 1997] in a region that is distinct from other mineral classes (Figures 3 and 4), and varies with cation composition [*Lane and Christensen*, 1997] (Figure 5a). A suite of rocks formed by hydrothermal precipitation and alteration in the Castle Hot Springs Volcanic Field of central Arizona is shown in Figure 5b. The travertine samples are characterized by the absorption features typical of carbonates (calcite). The hydrothermal silica spectrum exhibits the major absorption features between 8 and 10 μm that are characteristic of crystalline quartz. The basalt sample is a potential analog for hydrothermal alteration on Mars. It contains small (<1 mm) calcite-bearing vesicles and veins, similar to those found in the SNC sample ALH84001 [*McKay et al.*, 1996]. The spectral feature between 6.0 and 7.1 μm (1600 and 1400 cm^{-1}) is due to carbonate, demonstrating that a small amount of carbonate (<5%) can be detected in volcanic rocks using thermal-IR spectra.

[19] Minerals that incorporate hydroxyl (OH)- anions into their structure give clues about the availability of water during their formation. The majority of such minerals are silicates, and most of these are in the phyllosilicate group (Figure 5c). The hydrous silicates have characteristic mid-IR features due to fundamental bending modes of (OH)-

Figure 5. (opposite) Individual minerals and rocks associated with aqueous formation and alteration. The individual spectra have been scaled and offset for clarity. These coarse particulate mineral samples have band depth (emissivity minima) relative to the nearby local emissivity maxima of ~0.4 to 0.8. (a) Selected examples of minerals in the carbonate mineral group. (b) Thermal emission spectra of hydrothermal rocks. The travertine and hydrothermal quartz samples are from a hot-spring system within a volcanic environment. The hydrothermally altered basalt sample contains small (<1 mm) calcite-bearing vesicles, demonstrating that <5% carbonate can be detected in volcanic rocks. (c) Selected examples of minerals in the phyllosilicate mineral group.

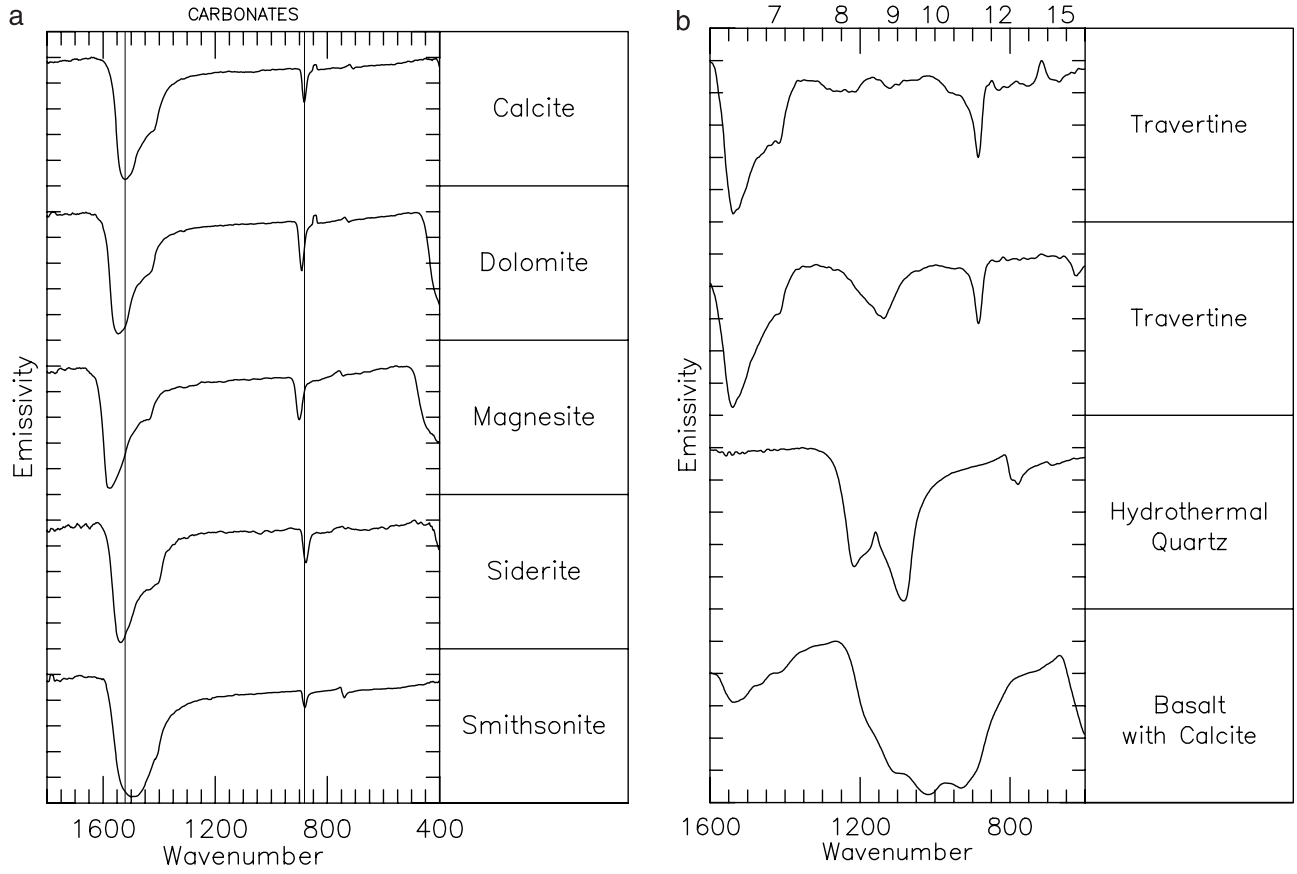
a
CARBONATES
Calcite
Dolomite
Magnesite
Siderite
Smithsonite
Emissivity
1600
1200
800
400
Wavenumber
b
7
8
9
10
12
15
Travertine
Travertine
Hydrothermal Quartz
Basalt with Calcite
Emissivity
1600
1200
800
Wavenumber
c
CLAYS
Kaolinite
Halloysite
Dickite
Montmorillonite
Nontronite
Fe–Smectite
Emissivity
1200
800
400
Wavenumber

attached to various metal ions, such as an AL-O-H bending mode near 11 μm in kaolinite clay [e.g., *Farmer*, 1974; *Van der Marel and Beeutelspacher*, 1976]. Though all the hydrous silicates have the hydroxyl anion, they range widely in their mode of occurrence. Some form as primary constituents of igneous rocks, giving clues about the magmatic conditions under which the rock was formed. Most hydrous silicates crystallize as secondary products of aqueous alteration and their composition provides insight into the pressure and temperature where they formed.

3.3. Quantitative Analysis of IR Spectra

[20] A key strength of mid-infrared spectroscopy for quantitative mineral mapping lies in the fact that mid-infrared spectra of mixtures typically are linear combinations of the individual components [*Thomson and Salisbury*, 1993; *Ramsey and Christensen*, 1998; *Feely and Christensen*, 1999; *Hamilton and Christensen*, 2000]. The mid-IR fundamental vibration bands have very high absorption coefficients and therefore much of the emitted energy only interacts with a single grain. When absorption coefficients are low, as is the case for overtone/combination bands, the energy is transmitted through numerous grains and the spectra become complex, non-linear combinations of the spectral properties of the mixture. The linear nature of the thermal spectral emission of mineral mixtures has been demonstrated experimentally in particulates >60 μm in size for mixtures of up to five components [*Thomson and Salisbury*, 1993; *Ramsey and Christensen*, 1998]. In these experiments the mineral abundance could be quantitatively retrieved using linear deconvolution techniques to within 5% on average.

[21] The linear mixing of mineral components in rock spectra has also been confirmed [*Feely and Christensen*, 1999; *Hamilton and Christensen*, 2000; *Wyatt et al.*, 2001; *Hamilton et al.*, 2001], with retrieved mineral abundances that are accurate to 5–10% in laboratory spectra. Mineral composition and abundance were determined both spectroscopically and using traditional thin-section techniques for a suite of 96 igneous and metamorphic rocks [*Feely and Christensen*, 1999]. The rocks were used in their original condition; no sample cutting, polishing, or powdering was performed, and weathered surfaces were observed where available to best simulate remote observations. Comparison of the mineral abundances determined spectroscopically with the petrographically estimated modes for each sample gave an excellent agreement using high-resolution data. The spectroscopically determined compositions matched the petrologic results to within 8–14% for quartz, carbonates, feldspar, pyroxene, hornblende, micas, olivine, and garnets. These values are comparable to the 5–15% errors typically quoted for traditional thin section estimates.

3.4. Environmental Effects

[22] Variations in particle size and porosity produce variations in the spectra of materials at all wavelengths. Numerous quantitative models have been developed to investigate these effects [*Vincent and Hunt*, 1968; *Hunt and Vincent*, 1968; *Conel*, 1969; *Hunt and Logan*, 1972; *Hapke*, 1981, 1993; *Salisbury and Eastes*, 1985; *Salisbury and Wald*, 1992; *Salisbury et al.*, 1994; *Moersch and Christensen*, 1995; *Wald and Salisbury*, 1995; *Mustard and Hays*, 1997; *Lane*, 1999] and have demonstrated the importance of specular reflectance and scattering. Two basic behaviors are observed with decreasing grain size: (1) strong bands (high absorption) tend to get shallower; and (2) weak bands (low absorption) increase in contrast, but appear as emission maxima and reflectance minima [*Vincent and Hunt*, 1968].

[23] Dust coatings and weathering rinds present a potential problem for any optical remotely-sensed measurements of Mars. However, the thickness of material through which sub-surface energy can escape increases linearly with wavelength. Thermal IR spectral measurements through coatings have been studied using mechanically deposited dust [*Ramsey and Christensen*, 1992; *Johnson et al.*, 2002] and terrestrial desert varnish [*Christensen and Harrison*, 1993] as analogs to Martian rock coatings. These results have shown that thermal-IR spectral observations can penetrate relatively thick (mean thickness up to ~40–50 μm) layers of these materials to reveal the composition of the underlying rock.

[24] Downwelling radiation is reflected off of the surface materials and this reflected component will be included in the total radiance received by the Mini-TES. The downwelling radiance will be measured directly using Mini-TES sky observations. It will also be modeled using MGS TES downward-looking observations of atmospheric temperature and dust, water-ice, and water-vapor abundances acquired simultaneously or at identical seasons from similar atmospheric conditions during previous Mars years [*Smith et al.*, 2001b].

4. Instrument Description

4.1. Instrument Overview

[25] The Mini-TES covers the spectral range from 5 to 29.5 μm (1997.06 to 339.50 cm^{-1}) with a spectral sampling of 9.99 cm^{-1}. A 6.35-cm-diameter Cassegrain telescope feeds a flat-plate Michelson moving mirror mounted on a voice-coil motor assembly that provides the optical path difference necessary for the Michelson interferometer while achieving excellent tilt performance. A single deuterated triglycine sulfate (DTGS) uncooled pyroelectric detector gives a spatial resolution of 20 mrad; a actuated field stop reduces the field of view to 8 mrad. The overall envelope size is 23.5 × 16.3 × 15.5 cm and the mass is 2.40 kg. The average power consumption is 5.6 W. Mini-TES I was delivered to JPL on Aug. 16, 1999, initially for integration into the 2001 Mars Lander; Mini-TES II was delivered on June 7, 2002. A summary of the instrument characteristics is given in Table 2.

[26] The Mini-TES spectrometer provides data to the rover computer at a fixed rate of one interferogram every two seconds (1.80 second Michelson scan, 0.20 second retrace) whenever it is powered. The rover flight software performs the Fast Fourier Transform (FFT) processing, spectral co-adding, and lossless compression. The FFT algorithm transforms the raw interferograms, containing up to 1120 16-bit interferogram samples, into 16-bit spectra during the 200 ms retrace period. The Mini-TES Zero-Path-Difference (ZPD) algorithm locates ZPD using a selectable choice of the positive-, negative-, or midpoint of the interferogram peak-to-peak amplitude, and selects the central 1024 points of the interferogram. The FFT generates a

Table 2. Mini-TES Design and Performance Parameters

Parameter	Description
Spectral Range	339.50 to 1997.06 cm^{-1} (5.01–29.45 μm)
Spectral Sampling Interval	9.99 cm^{-1}
Field of View	8 and 20 mrad
Telescope Aperture	6.35-cm-diameter Cassegrain
Detectors	Uncooled Alanine doped Deuterated Triglycine Sulphate (ADTGS) Pyroelectric detector
Michelson Mirror Travel	−0.25–0.25 mm
Mirror Velocity (physical travel)	0.0325 cm/sec
Laser Fringe Reference Wavelength	978 ± 2 nanometers
Interferometer Sample Rate	645 samples/sec
Cycle Time per Measurement	2 seconds (1.8 seconds Michelson mirror forward scan; 0.2 second retrace)
Number of Scans to Achieve 400 SNR at 1000 cm^{-1}; 270 K Scene Temperature; 0°C Instrument temperature	2 (20 mrad); 80 (8 mrad)
Number Samples per Interferogram	1024
Number Bits per Sample - Interferogram	16
Number Samples per Spectrum	167
Number Bits per Sample - Spectrum	12
Dimensions	23.5 × 16.3 × 15.5 cm
Mass	2.40 kg
Power	5.6 W (operating), 0.3 W (daily average)
Operational Temperature Range (Instrument Temperature)	Survival and Operability −45, +50°C; Performance within Spec −10, +30°C

spectrum of 512 16-bit samples, from which the 167 with useable response are selected. Co-addition of two spectra reduces the data rate by an additional factor of two, resulting in an average data rate of approximately 400 bits per second.

4.2. Optical/Mechanical Design

[27] The Mini-TES optical system (Figure 6) uses a compact Cassegrain telescope configuration with a 6.35-mm-diameter primary mirror that defines the system's aperture stop. Light reflects off the secondary mirror, forming the f/12 focal ratio. The 1.12-cm-diameter secondary obscures the clear aperture reducing the effective collection area. The use of baffles around the telescope housing and secondary mirror and the use of diffuse black paint around the optics and within the cavity minimize stray light effects. An anti-reflection coated Cadmium Telluride (CdTe) window is located between the exit of the telescope's optical path and the entrance of the interferometer optical system. This window is tilted so that an internal etalon is not created between this surface and the beamsplitter. A flat mirror folds the radiance into the plane of the interferometer. All mirror surfaces are diamond-turned and gold-coated.

[28] Mini-TES utilizes the identical Michelson interferometer design as the TES instruments. The radiance from the main fold mirror passes through a 0.635 cm thick Potassium Bromide (KBr) beamsplitter and its amplitude is split in two and reflected/transmitted to each arm of the interferometer. This beamsplitter is installed in a radial 3-point mount that allows the beamsplitter to maintain alignment over a 100°C operational range (−50°C to +50°C). Due to the hydroscopic nature of KBr, a dry nitrogen purge during ground testing is required to maintain its transmission properties. In order to maintain positive purge without over-pressurization, the Mini-TES housing has a CdTe window (described above), an exhaust port, and a check valve.

[29] A fixed mirror is in the reflected path of the interferometer, while a constant-velocity moving mirror is in the transmission path. The moving mirror moves ±0.25 mm to achieve the spectral sampling requirement of 10 cm^{-1}. The wave fronts recombine at the beamsplitter and pass through a compensator of identical thickness to the beamsplitter to preserve the optical path difference. This recombined radiance is directed by a fold mirror through the 20-mrad field stop toward the parabolic focus mirror. This mirror re-images the optical pupil onto the on-axis DTGS detector element, which is protected by thin (0.05 cm) chemical vapor deposited diamond window.

[30] A monochromatic fringe counting interferometer is used to precisely track the motion of the moving mirror assembly. The counting interferometer uses a redundant set of matched wavelength narrowband 978 nm laser diodes. The laser diodes are wavelength and temperature stabilized by the use of a Distributed Bragg Reflector (DBR) in a 1-meter fiber optic. There is a narrow thermal region where DBR lasers can be unstable and a small heater is provided to force the laser out of this region. The laser diode interference signal is measured at a silicon fringe counting detector, which has a neutral density filter over the detector element. The fringe counting interferometer was designed to provide 5 times oversampling of the shortest scene bandpass wavelength, resulting in a minimum of 964 samples for the total moving mirror distance.

[31] The instrument housing, interferometer optical bench, telescope and all optical mirrors are made of aluminum for light weight and strength, while meeting the launch load and MER pyro- and landing shock requirements. The Mini-TES housing has four mounting feet that serve as the mounting interface to the rover structure. The alignment of Mini-TES to the rover reference frame was performed using a removable alignment cube that was aligned to the Mini-TES optical axis and utilized precision registration surfaces to allow removal and installation to within the tolerance errors.

4.3. Electronics Design

[32] The block diagram of the Mini-TES flight electronics is shown in Figure 7. The interior of Mini-TES I is shown in Figure 8. Mini-TES uses two Datel DC to DC power converters that accept +11 to +36 volts unregulated

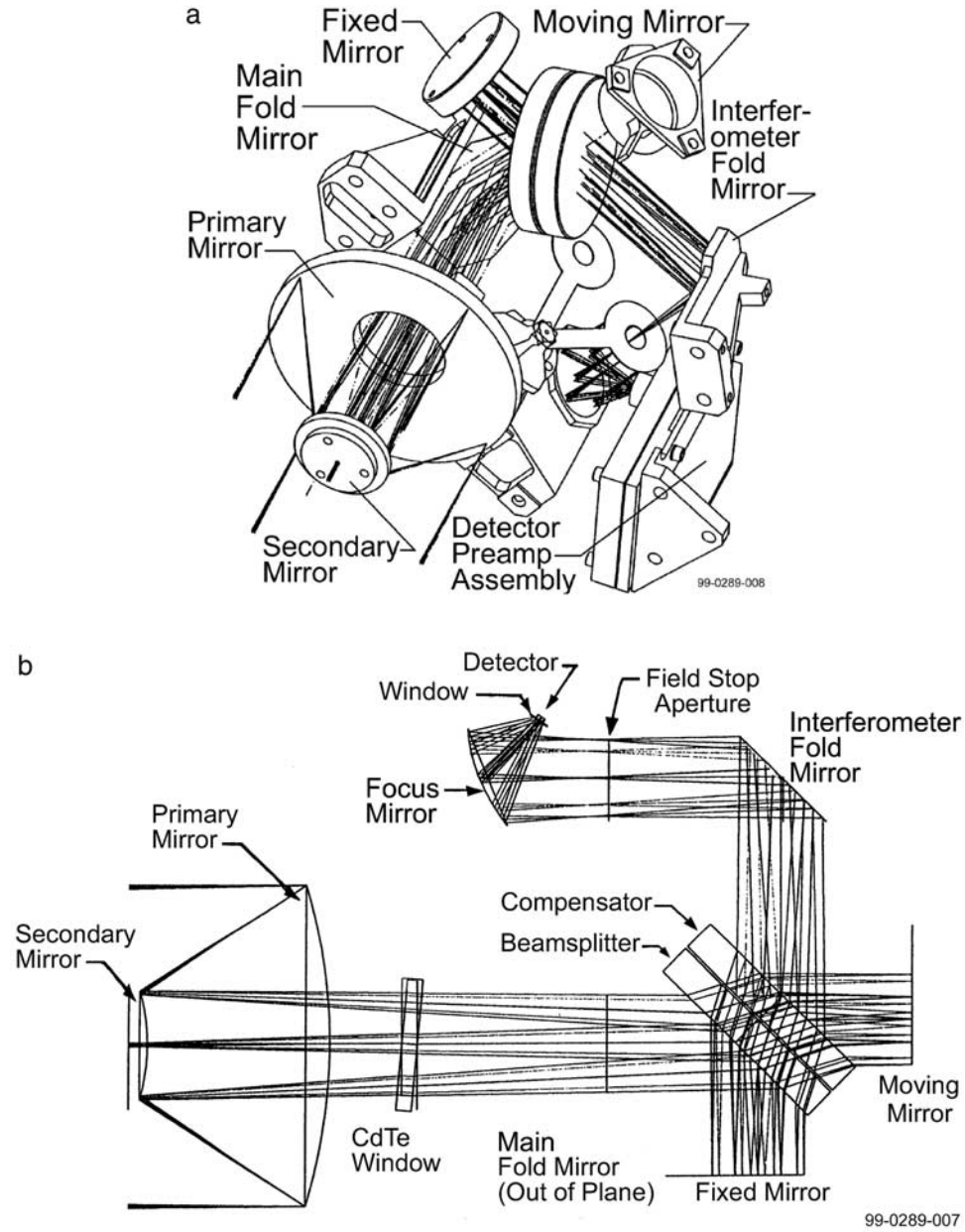

Figure 6. The Mini-TES optical system. (a) The Mini-TES 3-D perspective optical layout. Folding optics permit the full capabilities to be contained in a small lightweight package. (b) The Mini-TES optical design schematic. Schematic shows the unfolded optical system, including the Cassegrain collimating telescope, the interferometer, reimaging mirror and detector assembly, with a ray trace through all the elements.

input voltage and supply ±5 and ±15 volts regulated output voltage. The Datel converters went through significant screening by Raytheon and NASA to validate them for use on the MER Mini-TES instruments. The power converters are mounted on the same circuit card as the two SDL 80 mW 978 nm laser diode assemblies. These laser diodes have also been through significant screening for the Mini-TES instruments. The laser diodes are coupled into the optics via 1-m fiber optic cables. The power connections to the spacecraft power bus are through the 21-pin Cannon micro-D flight connector located at the base of the Mini-TES interferometer baseplate.

[33] Mini-TES uses an uncooled DTGS pyroelectric detector with an integrated FET detector package. The bias voltage applied to the FET by the pre-amplifier ensures that the DTGS detector's crystals are properly poled when power is applied to the instrument. Pre-amplification and front-end filtering is performed on the preamplifier circuit board to amplify the signal and to AC couple the detector output to block high frequency oscillations. A ±12 volt regulator supplies power to the detector and preamplifier electronics.

[34] The spectrometer circuit board performs the bulk of the analog electronics processing. The analog detector

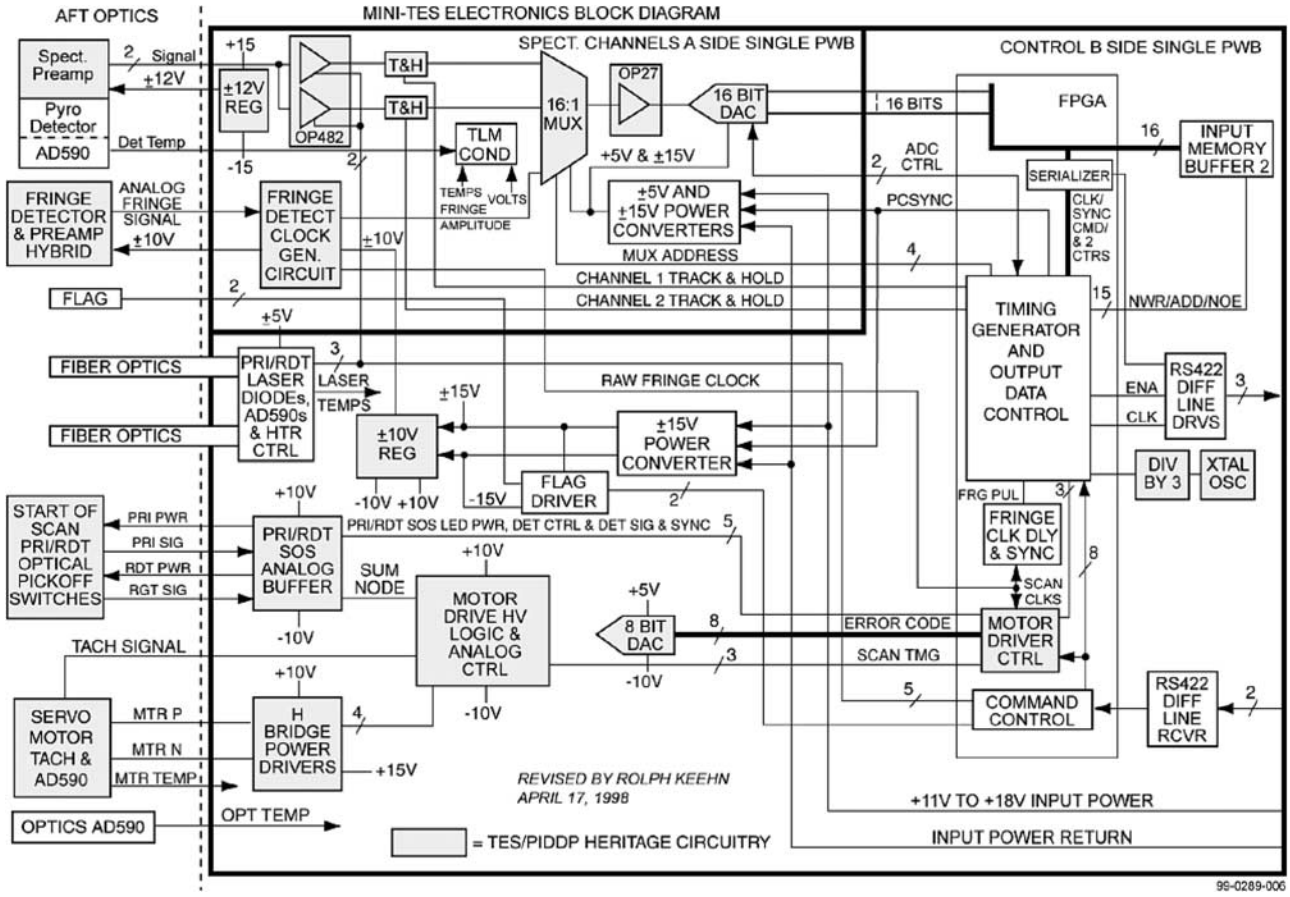

Figure 7. Block diagram of Mini-TES.

signal is passed through dual post-amplifier chains, performing the high-frequency boost, 3-pole Bessel filtering, amplifier gain, and analog signal track/hold. The interferogram signal due to the scene is ''boosted'' to account for the ''1/f'' roll-off of the detector response and is amplified to fill the 16-bit analog to digital converter. The filtering is performed to achieve the desired IR signal bandpass of 5 to 220 Hz. In addition, the analog signals from the two Hammamatsu silicone photo-diode fringe signal detectors are passed through the fringe post-amplifier

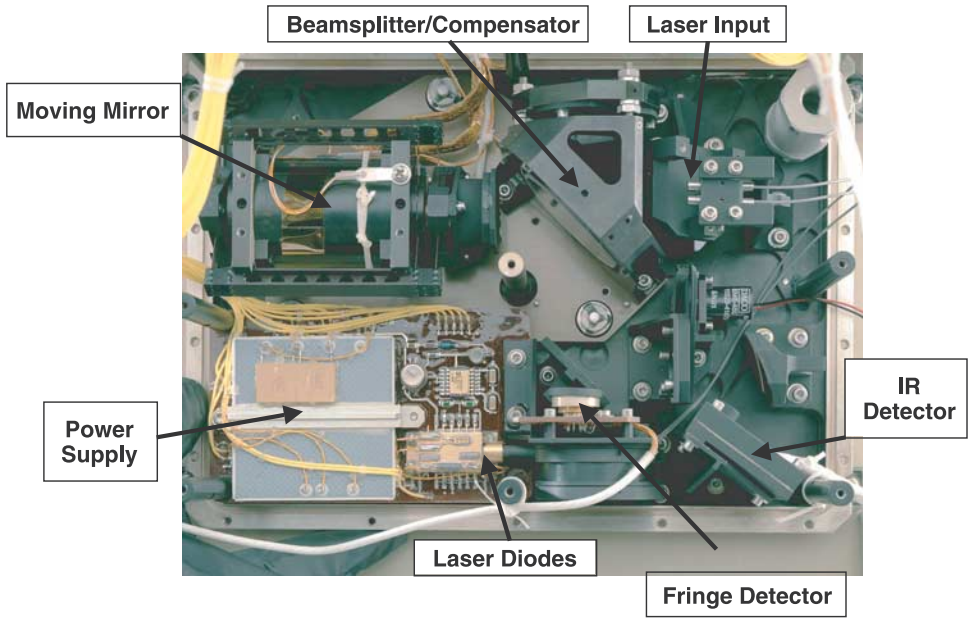

Figure 8. Interior view of the Mini-TES spectrometer components.

and fringe detection circuitry on the spectrometer board. The fringe detection electronics use a zero crossing comparator to generate the sampling pulse and the constant velocity servo feedback fringe clock. The amplified and filtered IR signal, fringe analog signal amplitude and the internal instrument analog telemetry is then fed into a 16:1 analog multiplexer followed by a 16-bit analog to digital converter. The 16-bit digital IR data are then transferred to the data buffer on the command and control circuit board for formatting and transfer to the Mini-TES interface electronics.

[35] The low level command, control and data flow tasks of the Mini-TES are controlled by logic in the command and control Field Programmable Gate Array (FPGA). The interface electronics parse out the low level instrument command parameters that control various Mini-TES hardware functions. The Mini-TES command parameters are: interferometer motor on/off, amplifier gain high/low, amplifier chain primary/redundant, target (shutter) open/close, laser diode1 on/off, laser heater2 on/off, start-of-scan optical switch primary/redundant, and laser heaters on/off.

[36] The flow of the digital interferometer data is controlled by additional logic in the command and control board FPGA. After each interferometer scan, the 16-bit interferogram data and 16-bit telemetry data are moved from the A/D to the input memory buffer on the 16-bit parallel data bus. These 16-bit parallel data are then sent to the digital multiplexer and serializer electronics where the three header words and fourteen digital telemetry words are serialized with the 16-bit IR data. The multiplexer, serializer and data formatting logic are included in the command and control FPGA. The three data header words include: 8-bit sync, 8-bit commanded parameter status, 16-bit scan count, and 16-bit interferogram sample count. The fourteen 16-bit telemetry words include: +5V power, −5V power, +15V power, −15V power, +10V power, −10V power, +12V power, −12V power, detector temperature, motor temperature, beamsplitter/optics temperature, laser diode1 temperature, laser diode2 temperature, and fringe signal amplitude.

[37] The Mini-TES timing sequencing electronics are implemented in the command and control board FPGA. These electronics generate the timing waveforms necessary to control and synchronize instrument operation. The timing electronics provide the control and synchronization of the amplification, track/hold, multiplexing, and analog to digital conversion of the analog signals. They also control and synchronize the interferometer servo electronics with the data acquisitions. The timing sequencing electronics include the fringe delay electronics which are used to correct the sampling error due to the phase delays between the fringe and IR analog channels. All clocks in the timing sequencer are generated from the master clock crystal oscillator which operates at a frequency of 14.5152 MHz.

[38] The Mini-TES interferometer servo electronics are located on the command and control board and include the digital motor control logic and the analog servo drive electronics. The interferometer digital drive electronics, located in the FPGA, receive scan timing clocks from the timing sequencer electronics and the fringe clock from the fringe detection electronics. The motor control logic uses these clocks to synchronize the mirror movement with the spectrometer data acquisitions. The interferometer analog servo drive electronics generate the analog signals that control the movement of the TES interferometer moving mirror actuator. The moving mirror uses a direct drive Schaeffer linear motor with tachometer feedback. The moving mirror tachometer signal is returned to the interferometer control electronics to allow active feedback control of the actuator. The start of scan is monitored using primary and redundant single and double scan optical-interrupters that are connected to the moving mirror assembly.

Table 3. Mini-TES Calibration Temperatures

	Instrument Temperature					
	−30°C		0°C		30°C	
Mini-TES I	BCU-1	BCU-2	BCU-1	BCU-2	BCU-1	BCU-2
	223K	145 K	253 K	145 K	190 K	325 K
		190 K		235 K		
		235 K				
		280 K				
		325 K				
Mini-TES II	BCU-1	BCU-2	BCU-1	BCU-2	BCU-1	BCU-2
	223 K	145 K	253 K	145 K	283 K	145 K
		235 K		235 K		235 K
		325 K		325 K		325 K

5. Instrument Calibration

5.1. Calibration Overview

[39] The initial Mini-TES calibration and test was performed at SBRS prior to delivery to JPL, and a subset of these tests was performed on the integrated Mini-TES/PMA assembly. The objectives of these tests were to determine (1) the field-of-view definition and alignment, (2) the out-of-field response, (3) the spectrometer spectral line shape and spectral sample position, and (4) the spectrometer radiometric calibration.

[40] Bench-level testing of the Mini-TES instrument was performed at SBRS in two phases. The first phase consisted of piece-part and system-level testing of the spectral performance of each sub-section under ambient conditions. The second phase consisted of field of view and out-of-field tests conducted before and after vibration and thermal-vacuum testing to determine and confirm the instrument field-of-view and alignment. Mini-TES I was operated for a total of 166 hours and Mini-TES II was operated for 594 hours at SBRS prior to initial delivery to JPL.

[41] The Mini-TES spectrometer, without the PMA, was tested and calibrated in vacuum at SBRS at instrument temperatures of −30, −10, 10, and 30°C. A matrix of calibration tests were performed viewing two precision calibration reference blackbody standards, one set at 223 K, 243 K, 263 K, and 283 K, while the second was varied at temperatures of 145 K, 190 K, 235 K, 280 K, and 325 K. The Mini-TES/PMA systems were radiometrically calibrated in 6 mbar of nitrogen at instrument temperatures of −30, 0, and 30°C over a range of calibration blackbody temperatures (Table 3). These tests determined (1) the emissivity and effective temperature of the internal reference surface, (2) the instrument response function and its variation with instrument temperature, (3) the absolute radiometric accuracy, (4) the spectrometer noise characteristics, and (5) the spectrometer gain values.

5.2. Calibration Targets

[42] The two precision calibration reference blackbody standards (BCU-1 and BCU-2) used in the thermal vacuum

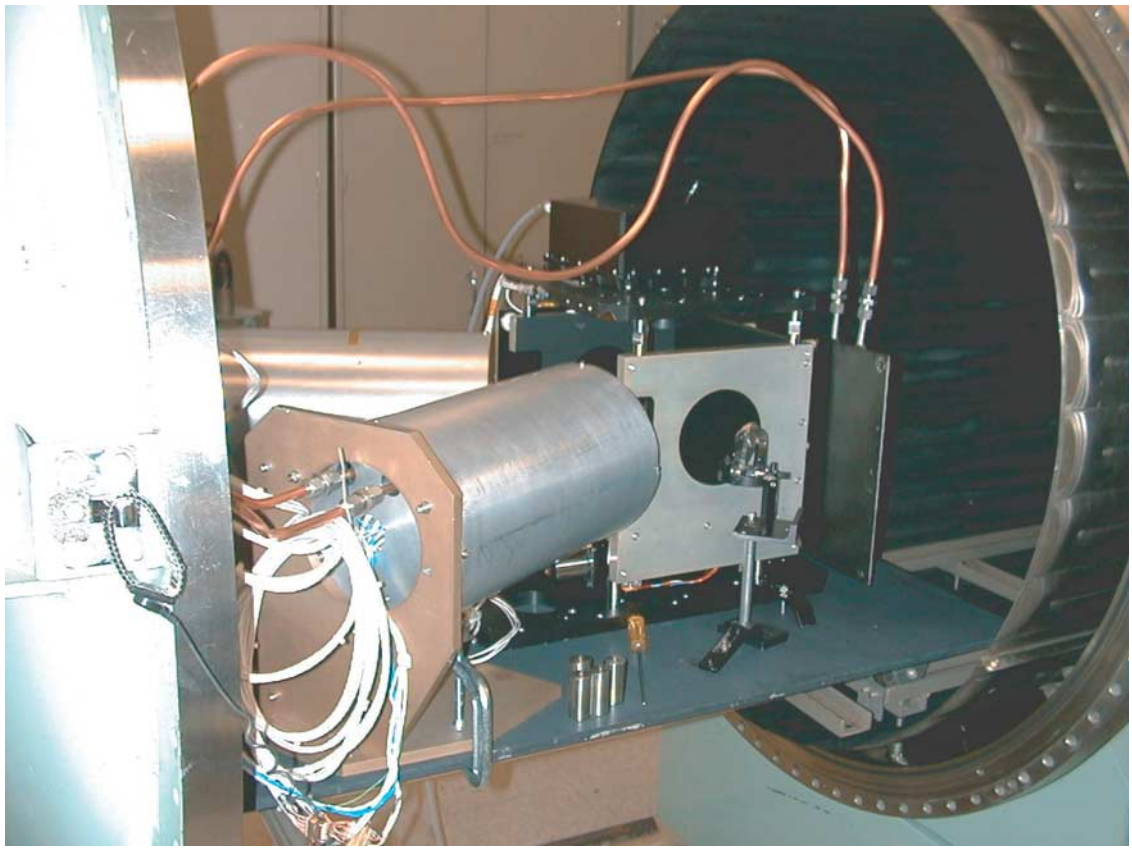

Figure 9. Mini-TES thermal vacuum test setup at Santa Barbara Remote Sensing. The Mini-TES instruments were tested at vacuum using precision calibration reference blackbodies. The cylindrical aluminum exterior of the two reference blackbodies can be seen in this image, along with Mini-TES (black box) that is pointing downward toward a pointing mirror that permitted the two reference blackbodies, a V-groove target (not visible) and a quartz crystal to be viewed.

calibration were identical, 7.25″ diameter, 15° half-angle cones machined at ASU and assembled and painted at SBRS. These targets are shown in Figure 9 in the thermal vacuum chamber at SBRS before the installation of the thermal blankets. Each blackbody was instrumented with two pairs of platinum thermistors, with one pair placed near the apex of the cone and the second pair approximately halfway between the apex and the opening of the cone. These thermistors were calibrated prior to shipment from the manufacturer to an absolute accuracy of 0.1°C (±0.5% resistance). The digitization of the reference blackbody telemetry points varies from ∼0.01°C at −190°C to 0.02°C at 35°C [*Christensen*, 1999; *Christensen et al.*, 2001a]. The temperature stability was within these digitization levels over >1 minute time periods. The front and back temperatures agree to within 0.7°C for cold temperatures, increasing to 1.5°C for hot temperatures.

[43] The Mini-TES internal and external flight calibration targets are formed with parallel grooves machined with 15° inclined surfaces with a depth of 1.73 mm and a spacing of 1.2 mm. The reference surface was machined from aluminum alloy and painted with Aeroglaze Z302 blank paint to a thickness of ∼6 mil.

[44] The external target will be exposed to the Martian atmosphere and will collect airfall dust during the mission. Dust build up can affect the emissivity of this target, although the geometric (e.g., V-groove) character provides a high emissivity regardless of the nature of the target surface. Immediately following landing both targets will be observed and used to determine the instrument response function. It is expected on the basis of TES data [*Christensen et al.*, 2001a] that the Mini-TES instrument response function will not vary significantly from its pre-launch value. In this case the pre-launch or initial landed instrument response function can be used throughout the mission, adjusted for instrument temperature, and adequate calibration can be obtained from a single point calibration using only the internal target.

[45] Each calibration target is instrumented with two platinum thermistors that are bonded to the underside. These thermistors were delivered from the manufacturer with a measured absolute accuracy of better than 0.1°C for temperatures from −130°C to 110°C. Resistances from the flight calibration target thermistors are digitized through the rover telemetry and converted to temperature. The digitization of the resultant temperatures is ∼0.02°C at 0°C. The temperature differences between the two independent temperature readings for each calibration target were determined during JPL thermal vacuum tests to be <0.5°C over the full range of operating temperatures.

[46] Immediately prior to launch one the internal reference thermistors in the MER-A PMA head failed. It was determined that the thermistors had been bonded incorrectly prior to delivery of the PMA to JPL in a manner that enhanced fracturing of the thermistor element. In response,

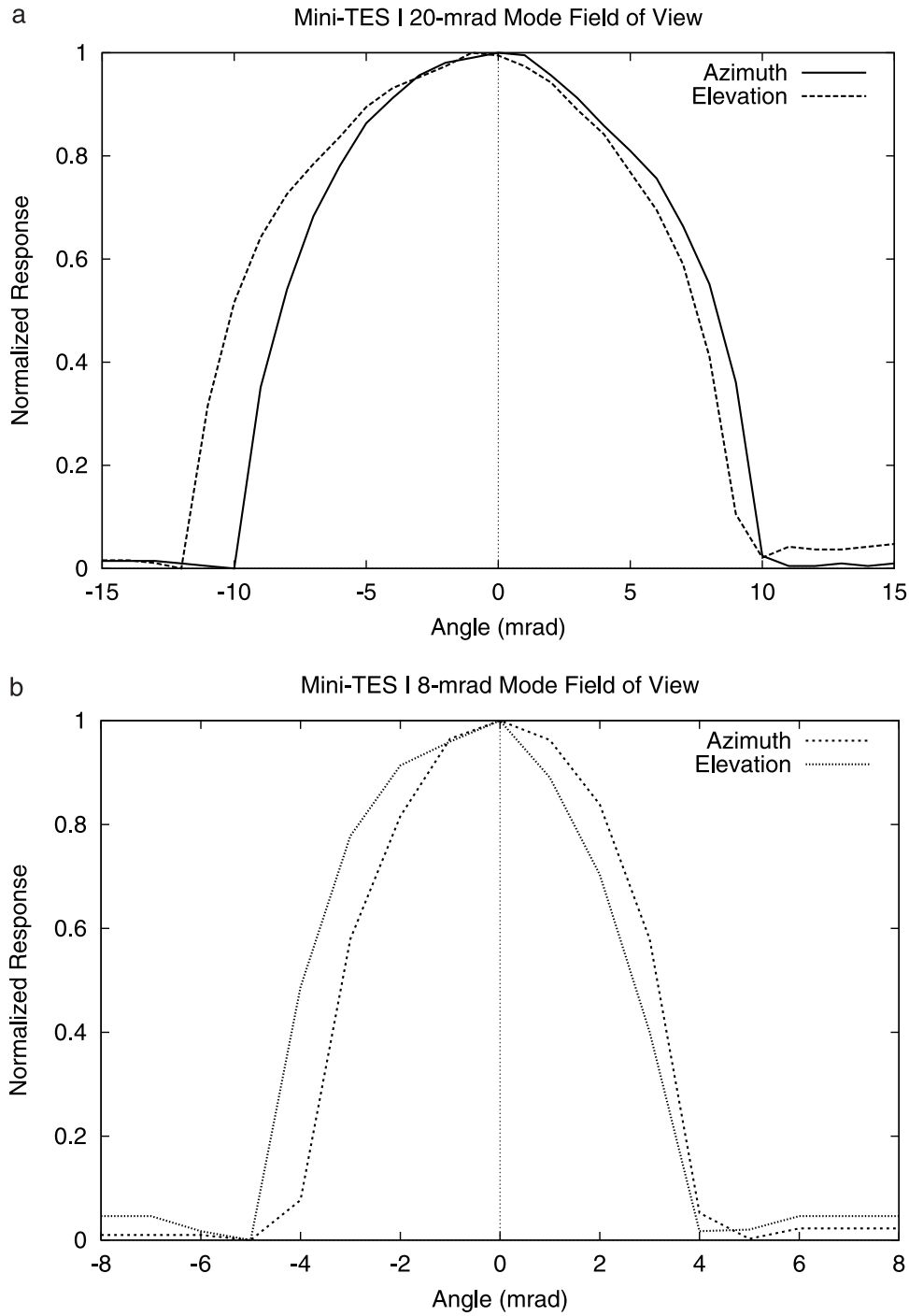

Figure 10. Mini-TES field of view. The response was mapped viewing a thermal source through a collimator and a 1 × 40-mrad slit that was stepped at 1-mrad increments across the aperture. (a) 20-mrad mode; (b) 8-mrad mode.

both PMAs were disassembled and one of the two thermistors on each assembly was replaced. This action preserved the pre-launch calibration for the remaining thermistor, while providing improved reliability.

5.3. Field of View

[47] Field of view characterization data were acquired at SBRS for the Mini-TES spectrometer using a precision collimator. Thermal and visual sources were projected through a 1 mrad wide, 40 mrad long slit into the Mini-TES aperture [*Christensen*, 1999]. The Mini-TES was manually rotated to move the slit at 1-mrad spacing across the focal plane; 31 points were measured from −15 to +15 mrad in elevation, 31 points were measured from −15 to +15 mrad in azimuth. The results from the final pre-shipment bench alignment tests for Mini-TES I in both 20- and 8-mrad mode in elevation and azimuth are shown in Figure 10. The FWHM of the Mini-TES 20-mrad field of

view mode is 17.5 mrad in azimuth and elevation. The FWHM of the 8-mrad field of view mode is 6.6 mrad in azimuth and 6.9 mrad in elevation. After the Mini-TES instruments were delivered to JPL, each was aligned to the PMA and tested to verify that the view is not vignetted by any elements of the PMA over the expected range of rover tilt angles.

[48] The near-field out-of-field response was measured at the bench level using a 2.4-mrad square slit that was stepped in 2.45 mrad increments from −14.7 to +14.7 mrad in azimuth and −19.6 to +19.6 mrad in elevation. The far-out-of-field response was determining over an extended area using a 40 × 32-mrad slit that was stepped in increments of 32.7 mrad in azimuth and 40 mrad in elevation from −196 to +196 mrad in azimuth and from −200 mrad to +200 mrad in elevation. No measurable out-of-field energy was detected in either test.

5.4. Radiometric Calibration

5.4.1. Overview

[49] For each observation the Mini-TES acquires an interferogram signal, measured in voltage, that is transformed to a signal as a function of frequency. This signal is given at each wave number (ν; subscripts omitted) by

$$V_{measured} = \{(R_{emitted} + R_{reflected}) - R_i\} * f \quad (1)$$

where

$V_{measured}$ is the Fourier-transformed voltage signal generated by the Mini-TES looking at the scene;
$R_{emitted}$ is the emitted radiance of the surface (W cm^{-2} sr^{-1}/cm^{-1});
$R_{reflected}$ is the background radiance reflected off of the surface (W cm^{-2} sr^{-1}/cm^{-1});
R_i is the radiance of the instrument (W cm^{-2} sr^{-1}/cm^{-1});
f is the instrument response function (V/W cm^{-2} sr^{-1}/cm^{-1}).

High emissivity targets (>0.995) were used for all of the calibration tests and the $R_{reflected}$ term can be ignored. Solving for the emitted radiance of the scene gives

$$R_{emitted} = \frac{V_{measured}}{f} + R_i \quad (2)$$

[50] During the system-level Mini-TES/PMA thermal-vacuum tests, observations were acquired of the two precision reference blackbody standards, one cold and one hot, and the flight external and internal calibration targets. The emitted radiance ($R_{emitted}$) of each target is given by εB, where ε is the emissivity of each target and B is the Planck function radiance at the target temperature. The relationships between the measured instrument signal (V) and the instrument and target radiance for the cold, hot, internal and external reference views are given by

$$V_{cold} = (\varepsilon_{cold} B_{cold} - R_i) * f \quad (3)$$

$$V_{hot} = (\varepsilon_{hot} B_{hot} - R_i) * f \quad (4)$$

$$V_{internal\ ref} = (\varepsilon_{internal\ ref} B_{internal\ ref} - R_i) * f \quad (5)$$

$$V_{external\ ref} = (\varepsilon_{external\ ref} B_{external\ ref} - R_i) * f \quad (6)$$

[51] The instrument response function has been shown through testing on the TES [*Christensen et al.*, 2001a] and Mini-TES to be independent of signal magnitude, but is a function of instrument temperature. The spectra from each target were acquired over a relatively short period of time (<3 min) under highly stable conditions with a constant instrument temperature, so R_i and f are assumed to be constant in equations (3)–(6). The temperature of the external targets and reference surface was determined to be constant to within 0.1°C using the thermistors located in or on each target surface, and the average temperature of each target over the time interval of data collection was used in the calibration.

[52] Equations (3) and (4) give two equations and four unknowns (ε_{cold}, ε_{hot}, R_i, and f). The calibration blackbodies have equal emissivities ($\varepsilon_{cold} = \varepsilon_{hot}$) that are >0.995 [*Christensen et al.*, 2001a; *Christensen*, 1999], and are assumed to be unity. With this substitution equations (3) and (4) give

$$f = \frac{V_{hot} - V_{cold}}{B_{hot} - B_{cold}} \quad (7)$$

and

$$R_i = R_{hot} - \frac{V_{hot}}{f} \quad (8)$$

5.4.2. Sample Position and Spectral Line Shape

[53] In an ideal interferometer with an on-axis point detector, the spectral samples are uniformly distributed in wave number and the full-width, half-maximum (FWHM) of each sample is determined by the optical displacement of the Michelson mirror. The Mini-TES uses a laser diode with a line at 0.978 μm in the visible interferometer to sample the IR interferometer. The ideal sample spacing of the interferometer is given by:

$$\text{Sample Spacing} = \frac{1}{(0.978 * 10^{-4}) * \text{Npts}} \quad (9)$$

where Npts is the number of points in the FFT and is equal to 1024 for the Mini-TES.

5.4.3. Flight Calibration Target Emissivity and Temperature

[54] The emissivity and temperature of the internal and external flight calibration targets were determined during thermal vacuum testing by computing the calibrated radiance from each target using equation (2), together with the R_i and f values determined by viewing the calibration reference standards. A Planck function was fit to the target calibrated radiance and the temperature of this best-fit function was assumed to be the kinetic temperature of the target. The target emissivity was determined using the ratio of the measured calibrated radiance to a blackbody at this kinetic temperature. The emissivity of the external target was also measured in the ASU Thermal Spectroscopy Lab. The temperature sensors on both targets were calibrated by comparing the derived kinetic temperature with the telemetry reading for each target. Analysis of these data is ongoing.

5.4.4. Radiometric Performance

[55] The instrument response varies with instrument temperature due to changes in detector response and interfer-

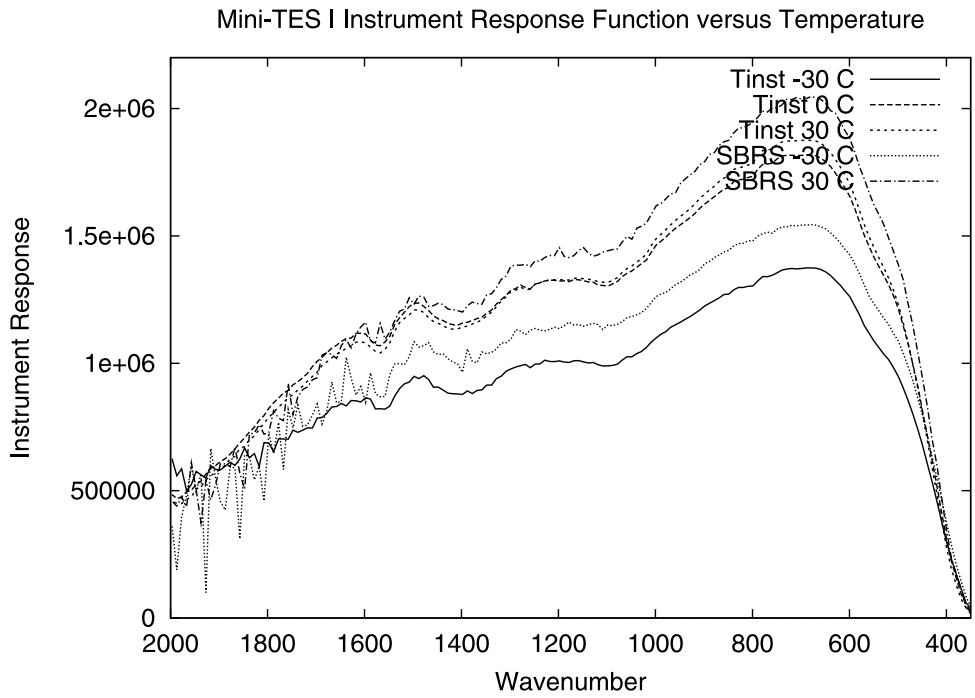

Figure 11. Variation in instrument response with temperature. The instrument response determined for the integrated Mini-TES I/PMA is shown for the three instrument temperatures (−30°C, 0°C, and +30°C) measured in 6 mbar of nitrogen at JPL. Also shown are the instrument response functions determined for the Mini-TES I spectrometer separately at SBRS.

ometer alignment with temperature. The variation of instrument response with temperature for is shown in Figure 11 for the system-level calibration tests done at JPL for Mini-TES I. The actual instrument response function will be determined in flight using observations of the internal and external calibration targets and equations (7) and (8).

[56] The noise equivalent spectral radiance (NESR) of the Mini-TES was determined in thermal vacuum testing by converting the standard deviation in signal to radiance using the instrument response function. This approach produces an upper limit to the noise levels (a lower limit to the SNR) because other sources of variance may be present that are not related to the instrument itself. The most likely of these are variations in the target radiance due to minor variations in target temperature.

[57] Figure 12 gives a representative NESR for Mini-TES I at instrument temperatures of −30, 0, and 30°C observing the internal reference surface. The 1-σ radiance noise level of an individual spectral sample in a single Mini-TES spectrum varies from 1.5 to 3.5 × 10^{-8} W cm^{-2} sr^{-1}/cm^{-1} for the central wave numbers from ∼450 to 1500 cm^{-1}, increasing to ∼6 × 10^{-8} W cm^{-2} sr^{-1}/cm^{-1} at shorter (300 cm^{-1}) and longer (1800 cm^{-1}) wave numbers (Figure 12). For the planned observing scenario in which two spectra are summed, these values reduce to 2.1 and 4.2 × 10^{-8} W cm^{-2} sr^{-1}/cm^{-1} respectively. As shown in Figure 11 the instrument response function decreases with decreasing temperature. However, the noise also decreases with temperature, so that there is only an approximately 35% increase in the noise level between the highest (30°C) and lowest (−30°C) instrument temperatures.

[58] The absolute calibration of the Mini-TES spectrometer was determined during thermal vacuum testing by computing the instrument response and instrument radiance using observations of the two precision calibration reference blackbodies. These values were used to convert observations of a separate V-groove target to calibrated spectral radiance using equation (2). An example of the comparison between the V-groove target calibrated radiance and the blackbody radiance computed using the measured V-groove temperature is given in Figure 13 for Mini-TES II at an instrument temperature of −10°C. Figure 13b shows the difference between the calibrated radiance and Planck function radiance at the measured V-groove temperature. At low scene temperatures (<220 K) there are errors of up to 2 × 10^{-7} W cm^{-2} sr^{-1}/cm^{-1} when comparing the derived calibrated radiance to the radiance calculated using the measured V-groove target temperature. However, the errors are less than 5 × 10^{-8} W cm^{-2} sr^{-1}/cm^{-1} when compared to the best-fit derived V-groove target temperature. On the basis of the quality of the best-fit Planck curves, we estimate that the primary error is in the calibration of the V-groove thermistors at low temperatures [*Christensen*, 1999; *Christensen et al.*, 2001a], and conclude that the absolute radiance error of the Mini-TES instrument is <5 × 10^{-8} W cm^{-2} sr^{-1}/cm^{-1}.

[59] Systematic errors in radiance can occur in the calibration process where noise in the internal and external calibration target observations is mapped into the calibrated scene spectra as a function of the instrument temperature and the temperature difference between the scene and the instrument. This noise will be reduced by acquiring and averaging ∼5 consecutive observations of both calibration targets.

[60] The Mini-TES temperature is expected to vary from −10 to +30°C over the course of a day, with most surface composition data collected at instrument temperatures >10°C

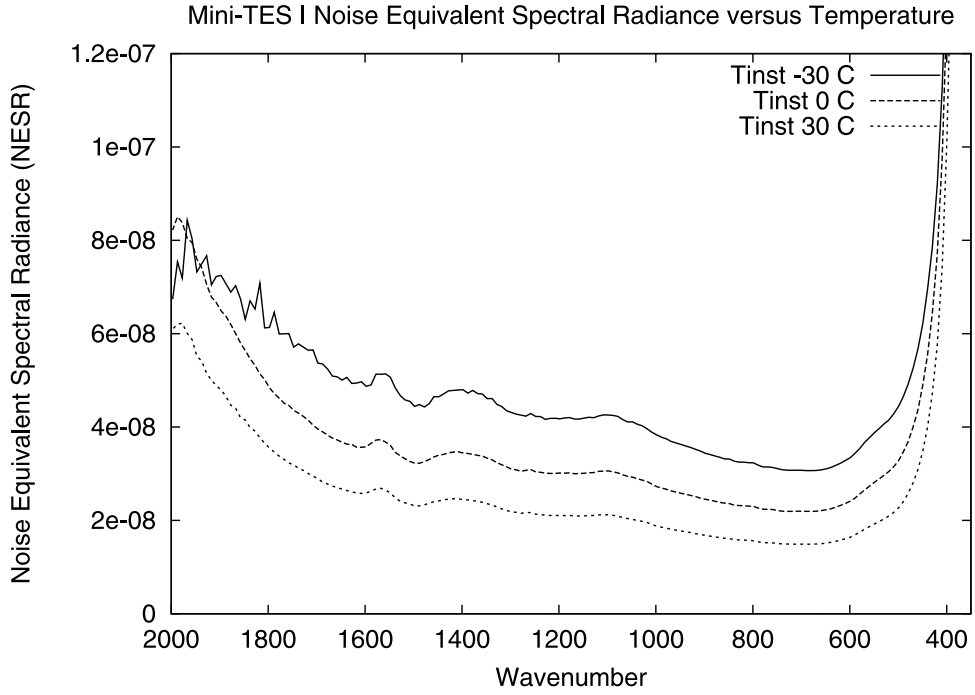

Figure 12. The noise equivalent spectral radiance (NESR) for the integrated Mini-TES I/PMA measured in 6 mbar nitrogen at JPL. Values are computed for a single spectrum. During operations at Mars two spectra will typically be averaged together, reducing the NESR by $\sqrt{2}$.

and scene temperatures >270 K. For this combination of temperatures, and assuming the nominal operational mode of the Mini-TES in which two spectra are collected for each observation, the radiometric precision is $\pm 1.8 \times 10^{-8}$ W cm^{-2} sr^{-1}/cm^{-1} between 450 and 1500 cm^{-1}. The absolute error, averaged over the wave number range where the scene temperature will be determined (1200–1600 cm^{-1}), will be $\sim 1 \times 10^{-8}$ W cm^{-2} sr^{-1}/cm^{-1} (Figure 13b). The worst-case sum of these random and systematic radiance errors correspond to a best-fit absolute temperature error of ~0.4 K for a true surface temperature of 270 K, and ~1.5 K for a surface at 180 K. This temperature error is mapped into a smoothly varying offset in the emissivity spectrum that varies from 0.001 at 400 cm^{-1}, to a maximum of 0.005 at ~1000 cm^{-1}, to essentially 0 at 1400 cm^{-1} for a scene temperature of 270 K. This subtle curvature has a negligible effect on the derived surface composition.

5.5. Rock Calibration Target Observations

[61] A rock calibration target containing 14 samples was constructed to provide mineral detection calibration and validation data for each of the MER science instruments [*Morris and Graff*, 2002; *Squyres et al.*, 2003]. The rocks ranged in size from 6.5 × 7.2 cm to 14.8 × 14.8 cm and were cut and polished. Both of the Mini-TES instruments viewed this target during system-level thermal vacuum testing at JPL. The target was placed 2.5 m from the Mini-TES telescope aperture, resulting in a projected, out-of-focus Mini-TES field of view of ~11.3 cm in size. A 41 × 33 raster image was obtained by Mini-TES I of roughly 3/4 of the target; test anomalies and time limitations only permitted the last column of rock targets to be observed with a single Mini-TES elevation scan.

[62] The calibrated spectral radiance from the rock targets was determined using the instrument response and instrument radiance obtained viewing the two calibration reference blackbodies immediately prior to the rock target observations. This spectral radiance consists of the emitted radiance from the rocks and the radiance emitted by the environment and reflected off of the rocks (equation (1)). The reflected component was removed by approximating the emitted radiance from the environment (B_{env}) assuming Planck function emission at the temperature of the vacuum chamber walls (~0°C), and simultaneously solving for the emissivity (ε_{rock}) and reflectivity ($1 - \varepsilon_{rock}$) of each rock. With these substitutions equation (1) becomes

$$V_{rock} = \{(\varepsilon_{rock} B_{rock} + (1 - \varepsilon_{rock}) B_{env}) R_i\} * f \qquad (10)$$

Solving for the emissivity of the rock gives

$$\varepsilon_{rock} = \frac{\frac{V_{rock}}{f} + R_i - B_{env}}{B_{rock} - B_{env}} \qquad (11)$$

[63] A similar procedure will be performed at Mars using the measured or modeled atmospheric downwelling radiance as $\varepsilon_{env} B_{env}$ and solving for the emissivity of the surface rocks and soils.

[64] Examples of the rock emissivity spectra with the environmental radiance removed are given in Figure 14. These spectra represent averages of ~5 Mini-TES spectra acquired at an instrument temperature of 0°C viewing rock targets heated to ~35°C (310 K). Figure 14 also shows the spectra of the same rock targets measured in the ASU Thermal Spectroscopy Laboratory. This figure shows the excellent agreement between the laboratory and flight

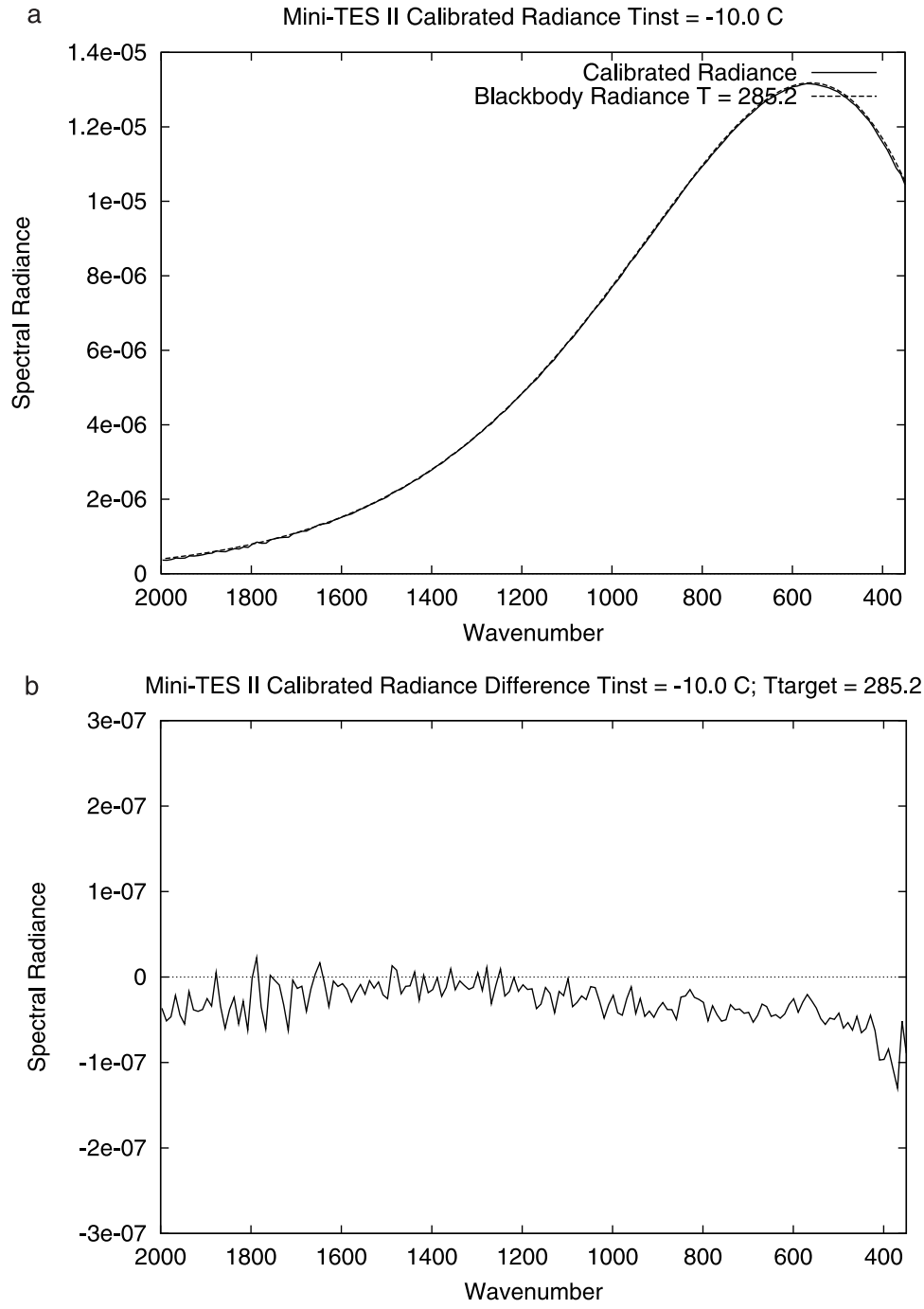

Figure 13. Absolute spectral radiance error. A representative example of the absolute radiance error for the Mini-TES I spectrometer is shown for an instrument temperature of 0°C measured in vacuum at SBRS. (a) Comparison of the derived calibrated spectral radiance viewing a V-groove target in thermal vacuum at SBRS and a Planck function fit to the calibrated radiance. (b) The difference between the V-groove calibrated spectral radiance and the best-fit Planck function.

instrument spectra, verifying the calibration and background radiance algorithms used for the Mini-TES instrument, and demonstrating the laboratory quality of the spectra that will be returned from Mars.

[65] Each of the rock targets was analyzed using the linear deconvolution method developed and used extensively for TES data analysis [*Adams et al.*, 1986; *Ramsey and Christensen*, 1998; *Christensen et al.*, 2000b]. A subset of 57 mineral spectra from the ASU thermal emission spectral library [*Christensen et al.*, 2000a] were selected for deconvolution of the rock target spectra. In addition, a high-silica glass spectrum was obtained along with additional goethite, magnesite, hematite, and chert samples. Two other end-members used in the subset were (1) a linear slope, to account for the variable brightness temperatures of the rock and rock mounting surface contained within the Mini-TES

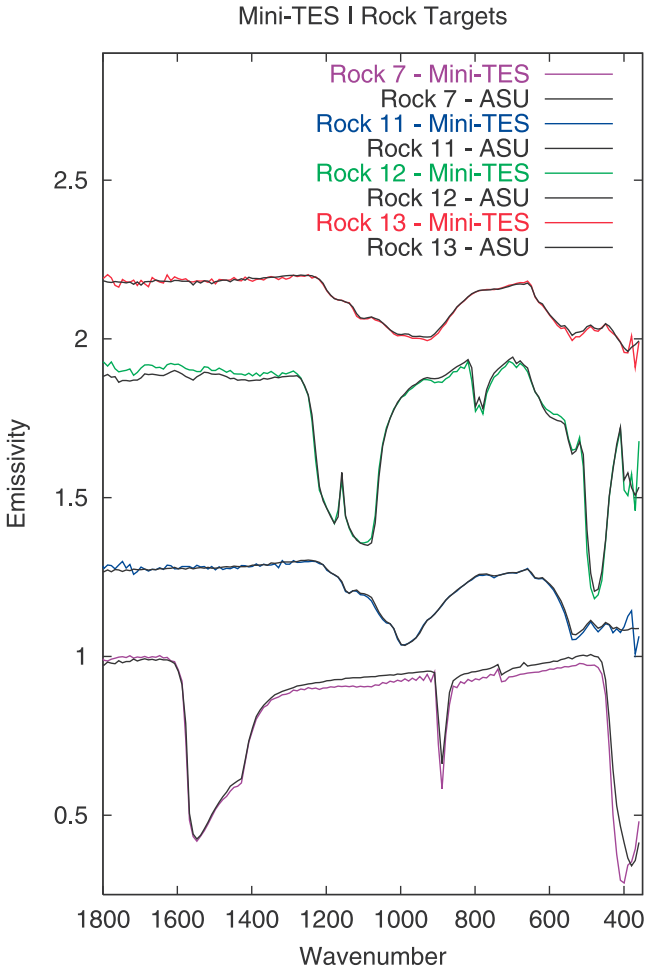

Figure 14. Mini-TES I spectra of selected rock targets. In all cases the Mini-TES field of view was larger than the rock target. The spectra shown here are averages of ~5 individual spectra. The reflected background radiance has been removed. These spectra illustrate the quality of spectra that will be obtained of the rocks and soils at the MER landing sites. Spectra from these rock targets obtained in the ASU Spectrometer Laboratory are shown for comparison.

field of view, and (2) blackbody (emissivity = 1.0), to account for spectral contrast differences between the particulate end-members in the ASU library (700–1000 μm) and polished rock slabs. Finally, the average emissivity spectrum from the first rock target was used as an end-member to deconvolve the mixed spectra from nearby samples due to a lack of mineral spectra that modeled this target well (corundum and blackbody were the best fit to this target, with RMS errors of ~12%). The extreme ends of each spectrum (339–399 cm^{-1} and 1727–1997 cm^{-1}) were excluded from the deconvolution, due to lower SNR in these spectral regions in both the measured and end-member emissivity. The band range used for each target was varied on the basis of model fits. Although different subsets of the end-member library were found to provide better fits for each target, the results reported here used the same 64-end-member set for each rock.

[66] The derived mineral abundances for each rock target are given in Table 4, normalized to remove the blackbody component. The individual model results have been grouped into the sum of each major mineral group. The slope end-member was used at the 1–2% level for all targets except Rock 4 (8%) and Rock 5 (3%). At the distance to the rock target the Mini-TES field of view was too large to completely resolve any individual target, and the emissivity includes components from surrounding targets and the background black paint. Examples of the measured and best-fit mineral mixture are shown in Figure 15. Future work will compare these analyses with mineral abundances measured using laboratory techniques as well as the composition of these rock targets determined from each of the other MER instruments.

6. Mission Operations

6.1. Observations

[67] The Mini-TES will be used in a number of different modes, one of the most important of which will be to acquire panoramas that will be co-registered with Pancam to provide merged mineralogic and morphologic information. A full 360°, 20-mrad panorama will be acquired while each rover is still on its lander, and other panoramas will be

Table 4. Mini-TES Rock Target Results

Mineral Abundance,[a] %	Rock Number												
	1	2	3	4	5	6	7	8	9	10	11	12	13
Feldspar		44	76	2		81	9	69	51	10	39		55
Pyroxene		2	5		8	6		2	3	1		2	17
Amphibole		2						16	3	11	39		
Olivine		12	6				10		6		9		9
Silica				9	61				4	4		36	
Oxide	100	12	9	61	16	9	13	6	7	54	1	58	8
Carbonate		1	1	1	2	1	67	1	1	16	2	4	1
Sheet-silicates		12	2		10	1		2	2	1	5	1	7
Apatite		1		12					5				
Al2SiO5				5				1					
Pyroxenoid											2		
High-Si Glass									16				
Garnet		2	1			1					2		3
Epidote		6				1		4	3	2			
Sum	100	94	100	90	97	100	99	101	101	99	99	101	100
Blackbody	0	−97	−45	−15	28	−136	−55	−94	19	−15	−85	−169	−76
RMS Error	0.000	0.714	0.470	0.549	1.290	0.691	3.225	0.494	0.355	0.520	0.748	1.694	0.720

[a]Abundances are normalized for blackbody and rounded to the nearest whole percentage.

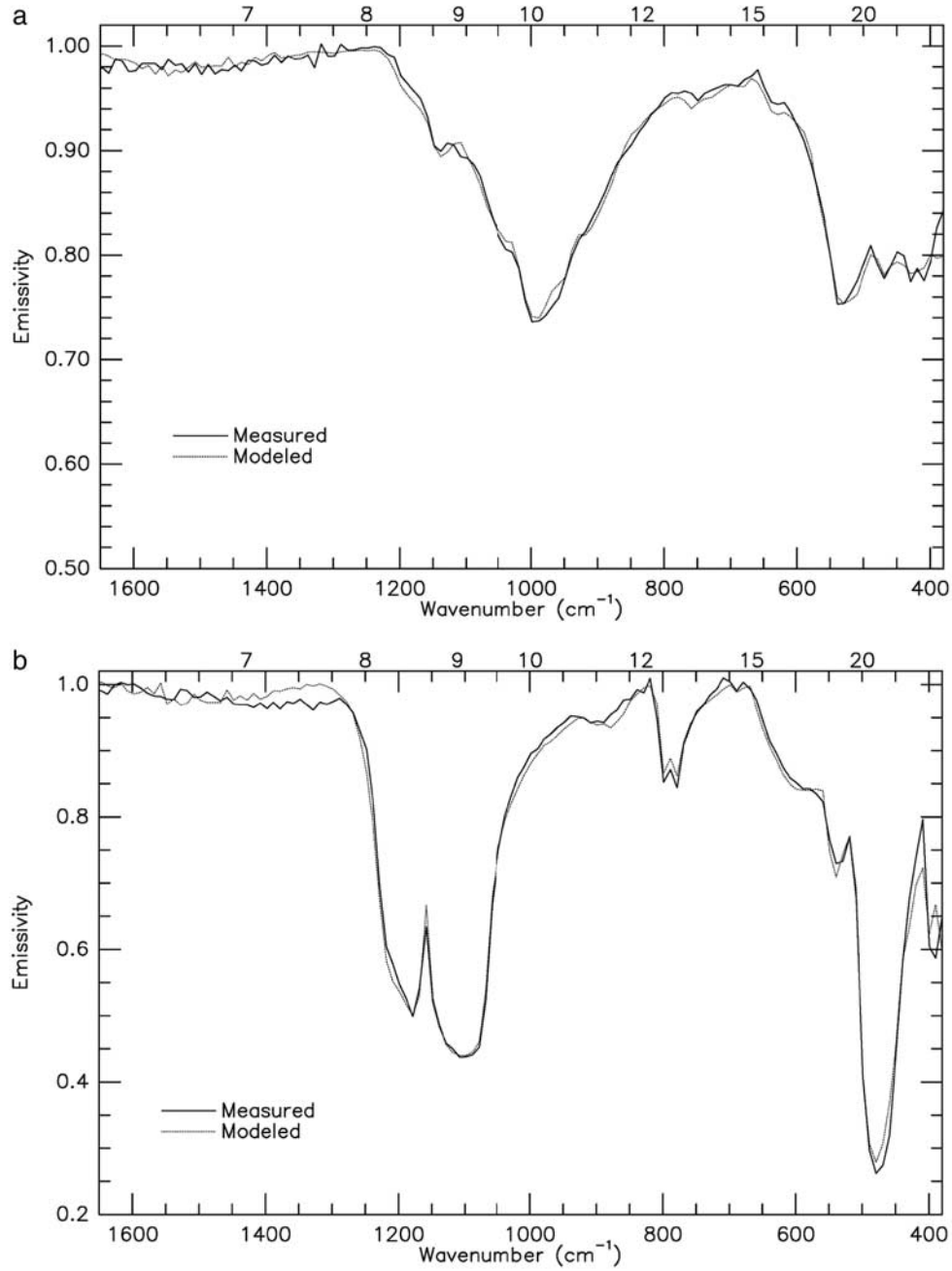

Figure 15. Mineral deconvolution results for selected rock targets. The modeled spectra were determined using a linear deconvolution technique and a library of 62 spectra (see text for details). The model spectra fit the measured spectra to within the noise of the Mini-TES instrument. The derived mineral abundances are given in Table 4. (a) Rock Sample 11. (b) Rock Sample 12. (c) Rock Sample 13.

obtained as appropriate as the rovers traverse the surface. In addition, Mini-TES will be operated in the 8-mrad field of view mode to obtain spectra from small raster scans of specific rock and soil targets.

[68] Limitations in Mini-TES observing time may require compromises when acquiring some panoramas. The elevation range can be restricted, typically to the region between the horizon and about 30° below. A single spectrum per pixel in 20-mrad mode can be used during the warmest times of day. It is also possible to use a raster step size of more than 20 mrad in one or both axes, undersampling the scene but providing more rapid coverage.

[69] Partial panoramas (i.e., rasters smaller than 360° in azimuth) will be an important use of Mini-TES. They typically will be targeted at regions of high scientific interest, on the basis of prior observations. Where appropriate, single column, row, or even single spot rasters will be targeted to address specific scientific hypotheses. In all instances the Mini-TES surface observations will be concentrated in the hottest part of the day when emission is

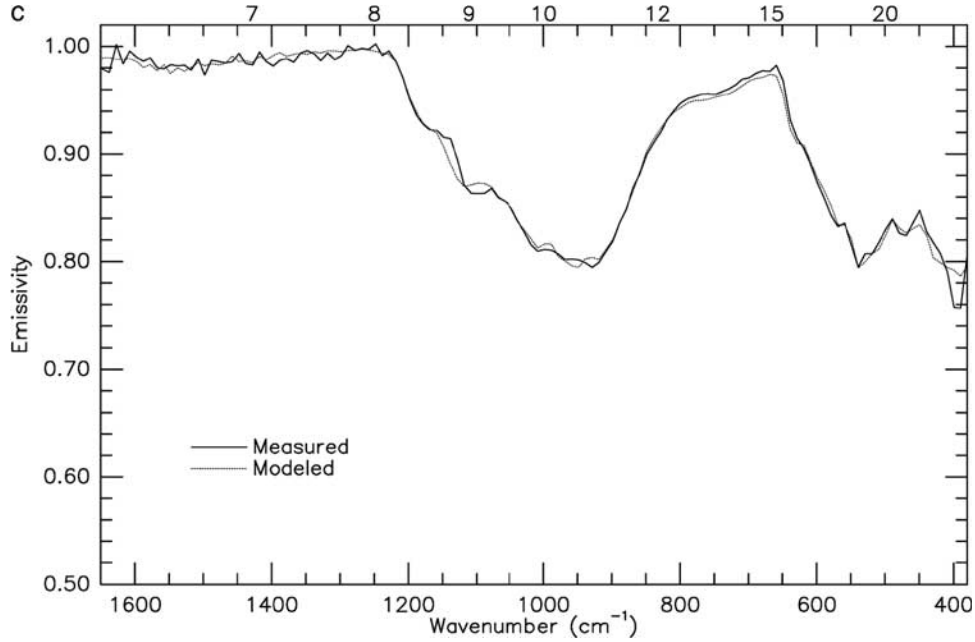

Figure 15. (continued)

highest, taking advantage of illumination geometry to view targets when they receive the most solar input, and using one spectrum per pixel when possible.

[70] The instrument's 8-mrad mode will be used sparingly. The minimum size of the Mini-TES beam is limited by the 6.35-cm diameter of the instrument's telescope aperture. In the near-field the Mini-TES spot size is the aperture size plus the angular divergence. Therefore near the rover the difference in diameter between the 20-mrad beam and the 8-mrad beam is small. Because 8-mrad observations require co-adding 80 spectra to achieve an acceptable SNR, this mode will not be useful close to the rover. The 8-mrad mode will be used on mid-range to distant targets when the 2.5× improvement in spatial resolution will help to answer a question that cannot be addressed at lower resolution.

[71] Whenever the in situ instrument suite is used on a rock or soil target, Mini-TES coverage of the target will be obtained before the rover leaves it. In many instances this will require driving the rover backward a short distance and acquiring Mini-TES data on the target, since much of the in situ instrument suite work volume is not visible to Mini-TES. For such observations spatial resolution will be of particular importance. This is especially true when the Rock Abrasion Tool (RAT) has been used on the target, because the region exposed by the RAT is only 4.5 cm in diameter, or about half the size of the Mini-TES beam directly in front of the rover. These targets will be observed using substantial oversampling, stepping the pointing mirror at a fraction of the projected Mini-TES field of view and using spatial deconvolution techniques to sharpen the effective resolution.

6.2. In-Flight Calibrated Radiance Algorithm

[72] The objectives of the in-flight calibration are (1) to develop an effective means for interpolating the instrument response function and instrument radiance between calibration observations and (2) to minimize the noise on these functions by taking advantage of their repetitive and predictable forms. The instrument radiance and the response function are determined using simultaneous observations of the internal (I) and external (E) calibration targets (''IE-pairs''). The response function is slowly varying except for small variations due to changes in instrument temperature, whereas R_i can vary continuously throughout the day. Thus IE-pairs will be acquired only at the start and end of each observing sequence to determine the response function, while the internal calibration target will be observed approximately every 3–5 minutes to determine R_i.

[73] Initially the response function for each scene observation will be determined using a linear interpolation between the response functions for bounding IE-pairs. However, the noise in the response function from a single IE-pair can be reduced by combining multiple determinations over a period of time, taking into account the changes due to variations in instrument temperature. During the mission, the data will be recalibrated using a low-noise response function determined by fitting a function to the complete set of instrument response data over long (∼10 day) periods. Once the instrument radiance is determined for each internal calibration target observation, it will be interpolated over time for all of the intervening scene observations and used with the response function to determine the calibrated radiance for each scene spectrum (equation (2)). Initially a linear interpolation between bounding values will be used; with time a more complex function will be determined to account for repetitive, periodic variations in instrument temperature.

[74] The following sequence of operations will be carried out for radiometric calibration:

[75] 1. Identify all of the Internal/External calibration target (IE) pairs and Internal target observations (I) associated with a given observation.

[76] 2. At each IE-pair, compute the radiance of the instrument (R_i), the instrument response function (f), and

the temperature of the instrument (T_i) using equations (7) and (8).

[77] 3. At each Internal observation, compute R_i by using the measured spectrum and f determined by interpolating over time between bounding IE-pairs.

[78] 4. At each scene observation, determine f and R_i by interpolating over time between the bounding IE-pair or I observations, and compute R_s for each detector using equation (2).

6.3. Data Products

[79] The Mini-TES calibrated radiance is the primary data product for the MER mission. These data will be converted to effective emissivity and surface temperature by fitting a Planck blackbody function to the calibrated spectrum. The emissivity spectra will be converted to mineral abundance using a linear deconvolution model [*Adams et al.*, 1986; *Ramsey and Christensen*, 1998] and a matrix of mineral spectra from the ASU Mineral Library [*Christensen et al.*, 2000a] and other sources. The derived surface temperature will be used to produce thermal inertia images via a thermal model [e.g., *Kieffer et al.*, 1977], using data from multiple times of day where possible. Attempts will be made to coordinate these diurnal observations with the times of TES or THEMIS direct overflights, providing simultaneous temperature observations that can be extended to broader regions surrounding the rovers.

[80] The Mini-TES will also view upward at angles up to 30° above the horizon to provide high-resolution temperature profiles of the Martian boundary layer [*Smith et al.*, 1996]. This upward-viewing mode will yield high-resolution temperature profiles through the bottom few km of the atmosphere using temperatures retrieved from the wings of the 15-μm CO_2 band. This lowest region of the atmosphere has been difficult to measure on Mars because of the nature of the weighting functions as seen from orbit, and because of the difficulty of determining surface contributions to radiance.

[81] Atmospheric water abundance will be obtained by vertical and horizontal viewing of rotational H_2O lines. Separate measurements of water near the ground will be obtained by viewing distant surface obstacles. The broad water-ice feature centered near 800 cm^{-1} [*Curran et al.*, 1973; *Pearl et al.*, 2001] will allow monitoring of ground ice hazes. Together, these measurements will illuminate the behavior of water in lower atmosphere and of water transport between the atmosphere and surface. Atmospheric dust abundance will be obtained using the redundant temperature information in both sides of the 15 μm CO_2 band, together with differential absorption across the dust band in that region.

[82] **Acknowledgments.** The Mini-TES was developed under funding from NASA's Planetary Instrument Definition and Development Program, Mars 2001 Lander, and Mars Exploration Rover Projects. We wish to thank all those involved at Arizona State University, Raytheon Santa Barbara Remote Sensing, the Jet Propulsion Laboratory, and Ball Aerospace in the development of the Mini-TES and Pancam Mast Assembly. Laura Aben, Robin Ferguson, Timothy Glotch, Trevor Graff, Amy Knudson, Deanne Rogers and Steve Ruff made significant contributions to the thermal vacuum testing and calibration at SBRS and JPL; Trevor Graff helped in the development of the rock targets; Deanne Rogers and Josh Bandfield contributed to the rock compositional analysis. The paper was improved through the detailed reviews by Wendy Calvin and Melissa Lane.

References

Adams, J. B., M. O. Smith, and P. E. Johnson, Spectral mixture modeling: A new analysis of rock and soil types at the Viking Lander 1 site, *J. Geophys. Res.*, *91*, 8098–8112, 1986.

Bandfield, J. L., Global mineral distributions on Mars, *J. Geophys. Res.*, *107*(E6), 5042, doi:10.1029/2001JE001510, 2002.

Bandfield, J. L., V. E. Hamilton, and P. R. Christensen, A global view of Martian volcanic compositions, *Science*, *287*, 1626–1630, 2000.

Bartholomew, M. J., A. B. Kahle, and G. Hoover, Infrared spectroscopy (2.3–20 μm) for the geological interpretation of remotely-sensed multispectral thermal infrared data, *Int. J. Remote Sensing*, *10*(3), 529–544, 1989.

Bell, J. F., III, and R. V. Morris, Identification of hematite on Mars from HST, *Lunar Planet. Sci.*, *XXX*, abstract 1751, 1999.

Christensen, P. R., *Calibration Report for the Thermal Emission Spectrometer* (*TES*) for the Mars Global Surveyor Mission, 228 pp., Mars Global Surveyor Proj., Jet Propul. Lab., Pasadena, Calif., 1999.

Christensen, P. R., and S. T. Harrison, Thermal infrared emission spectroscopy of natural surfaces: Application to desert varnish coatings on rocks, *J. Geophys. Res.*, *98*(B11), 19,819–19,834, 1993.

Christensen, P. R., et al., Thermal Emission Spectrometer experiment: The Mars Observer Mission, *J. Geophys. Res.*, *97*, 7719–7734, 1992.

Christensen, P. R., J. L. Bandfield, V. E. Hamilton, D. A. Howard, M. D. Lane, J. L. Piatek, S. W. Ruff, and W. L. Stefanov, A thermal emission spectral library of rock forming minerals, *J. Geophys. Res.*, *105*, 9735–9738, 2000a.

Christensen, P. R., J. L. Bandfield, M. D. Smith, V. E. Hamilton, and R. N. Clark, Identification of a basaltic component on the Martian surface from Thermal Emission Spectrometer data, *J. Geophys. Res.*, *105*, 9609–9622, 2000b.

Christensen, P. R., et al., Detection of crystalline hematite mineralization on Mars by the Thermal Emission Spectrometer: Evidence for near-surface water, *J. Geophys. Res.*, *105*, 9623–9642, 2000c.

Christensen, P. R., et al., The Mars Global Surveyor Thermal Emission Spectrometer experiment: Investigation description and surface science results, *J. Geophys. Res.*, *106*, 23,823–23,871, 2001a.

Christensen, P. R., M. C. Malin, R. V. Morris, J. L. Bandfield, and M. D. Lane, Martian hematite mineral deposits: Remnants of water-driven processes on early Mars, *J. Geophys. Res.*, *106*, 23,873–23,885, 2001b.

Conel, J. E., Infrared emissivities of silicates: Experimental results and a cloudy atmosphere model of spectral emission from condensed particulate mediums, *J. Geophys. Res.*, *74*, 1614–1634, 1969.

Curran, R. J., B. J. Conrath, R. A. Hanel, V. G. Kunde, and J. C. Pearl, Mars: Mariner 9 spectroscopic evidence for H_2O ice clouds, *Science*, *182*, 381–383, 1973.

Farmer, V. C., *The Infrared Spectra of Minerals*, 539 pp., Mineral. Soc., London, 1974.

Feely, K. C., and P. R. Christensen, Quantitative compositional analysis using thermal emission spectroscopy: Application to igneous and metamorphic rocks, *J. Geophys. Res.*, *104*, 24,195–24,210, 1999.

Glotch, T. D., R. V. Morris, T. G. Sharp, and P. R. Christensen, Characterization of the effects of precursor mineralogy on hematite spectra: Application to Martian hematite mineralization, *Lunar Planet. Sci.*, *XXXIV*, abstract 2008, 2003.

Hamilton, V. E., Thermal infrared emission spectroscopy of the pyroxene mineral series, *J. Geophys. Res.*, *105*, 9701–9716, 2000.

Hamilton, V. E., and P. R. Christensen, Determination of modal mineralogy of mafic and ultramafic igneous rocks using thermal emission spectroscopy, *J. Geophys. Res.*, *105*, 9717–9734, 2000.

Hamilton, V. E., M. B. Wyatt, J. H. Y. McSween, and P. R. Christensen, Analysis of terrestrial and Martian volcanic compositions using thermal emission spectroscopy: II. Application to Martian surface spectra from MGS TES, *J. Geophys. Res.*, *106*, 14,733–14,747, 2001.

Hapke, B., Bidirectional reflectance spectroscopy I. Theory, *J. Geophys. Res.*, *86*, 3039–3054, 1981.

Hapke, B., Combined theory of reflectance and emittance spectroscopy, in *Remote Geochemical Analysis: Elemental and Mineralogical Composition*, edited by C. M. Pieters and P. A. J. Englert, pp. 31–42, Cambridge Univ. Press, New York, 1993.

Henderson, B. G., B. Jakosky, and C. E. Randall, A Monte Carlo model of polarized thermal emission from particulate planetary surfaces, *Icarus*, *99*, 51–62, 1992.

Hunt, G. R., and L. M. Logan, Variation of single particle mid-infrared emission spectrum with particle size, *Appl. Opt.*, *11*, 142–147, 1972.

Hunt, G. R. and J. W. Salisbury, Mid-infrared spectral behavior of metamorphic rocks, *Environ. Res. Pap., 543-AFCRL-TR-76-0003*, 67 pp., Air Force Cambridge Res. Lab., Hanscom Air Force Base, Mass., 1976.

Hunt, G. R., and R. K. Vincent, The behavior of spectral features in the infrared emission from particulate surfaces of various grain sizes, *J. Geophys. Res.*, *73*, 6039–6046, 1968.

Hynek, B. M., R. E. Arvidson, and R. J. Phillips, Geologic setting and origin of Terra Meridiani hematite deposit on Mars, *J. Geophys. Res.*, *107*(E10), 5088, doi:10.1029/2002JE001891, 2002.

Johnson, J. R., P. R. Christensen, and P. G. Lucey, Dust coatings on basaltic rocks and implications for thermal infrared spectroscopy of Mars, *J. Geophys. Res.*, *107*(E6), 5035, doi:10.1029/2000JE001405, 2002.

Kieffer, H. H., and T. N. Titus, TES mapping of Mars' north seasonal cap, *Icarus*, *154*, 162–189, 2001.

Kieffer, H. H., T. Z. Martin, A. R. Peterfreund, B. M. Jakosky, E. D. Miner, and F. D. Palluconi, Thermal and albedo mapping of Mars during the Viking primary mission, *J. Geophys. Res.*, *82*, 4249–4292, 1977.

Kieffer, H. H., T. Titus, K. Mullins, and P. R. Christensen, Mars south polar cap as observed by the Mars Global Surveyor Thermal Emission Spectrometer, *J. Geophys. Res.*, *105*, 9653–9700, 2000.

Lane, M. D., and P. R. Christensen, Thermal infrared emission spectroscopy of anhydrous carbonates, *J. Geophys. Res.*, *102*, 25,581–25,592, 1997.

Lane, M. D., and P. R. Christensen, Thermal infrared emission spectroscopy of salt minerals predicted for Mars, *Icarus*, *135*, 528–536, 1998.

Lane, M. D., Infrared optical constants of calcite and their relationship to particle size effects in thermal emission spectra of granular calcite, *J. Geophys. Res.*, *104*, 14,099–14,108, 1999.

Lazerev, A. N., *Vibrational Spectra and Structure of Silicates*, 302 pp., Consult. Bur., New York, 1972.

Lyon, R. J. P., Evaluation of infrared spectroscopy for compositional analysis of lunar and planetary soils, in *Stanford Research Institute Final Report Contract NASr*, pp. 13–41, Stanford Res. Inst., Stanford, Calif., 1962.

McKay, D. S., E. K. Gibson Jr., K. L. Thomas-Keprta, H. Vali, C. S. Romanek, S. J. Clemett, X. D. F. Chillier, C. R. Maechling, and R. N. Zare, Search for past life on Mars: Possible relic biogenic activity in Martian meteorite ALH84001, *Science*, *273*, 924–930, 1996.

McSween, H. Y., Jr., What have we learned about Mars from SNC meteorites?, *Meteoritics*, *29*, 757–779, 1994.

Moersch, J. E., and P. R. Christensen, Thermal emission from particulate surfaces: A comparison of scattering models with measured spectra, *J. Geophys. Res.*, *100*, 7465–7477, 1995.

Morris, R. V., and T. G. Graff, Athena instrument validation and data library development for the Mars Exploration Rover (MER) Mission, *Eos Trans. AGU*, *83*(47), Fall Meet. Suppl., abstract P21C-03, 2002.

Mustard, J. F., and J. E. Hays, Effects of hyperfine particles on reflectance spectra from 0.3 to 25 μm, *Icarus*, *125*, 145–163, 1997.

Nash, D. B., and J. W. Salisbury, Infrared reflectance spectra of plagioclase feldspars, *Geophys. Res. Lett.*, *18*, 1151–1154, 1991.

Pearl, J. C., M. D. Smith, B. J. Conrath, J. L. Bandfield, and P. R. Christensen, Observations of water-ice clouds by the Mars Global Surveyor Thermal Emission Spectrometer experiment: The first Martian year, *J. Geophys.*, 12,325–12,338, 2001.

Ramsey, M. S., and P. R. Christensen, The linear "un-mixing" of laboratory thermal infrared spectra: Implications for the Thermal Emission Spectrometer (TES) experiment, Mars Observer, *Lunar Planet. Sci.*, *XXIII*, 1127–1128, 1992.

Ramsey, M. S., and P. R. Christensen, Mineral abundance determination: Quantitative deconvolution of thermal emission spectra, *J. Geophys. Res.*, *103*, 577–596, 1998.

Ruff, S. W., P. R. Christensen, P. W. Barbera, and D. L. Anderson, Quantitative thermal emission spectroscopy of minerals: A technique for measurement and calibration, *J. Geophys. Res.*, *102*, 14,899–14,913, 1997.

Salisbury, J. W., Mid-infrared spectroscopy: Laboratory data, in *Remote Geochemical Analysis: Elemental and Mineralogical Composition*, edited by C. Pieters and P. Englert, chap. 4, pp. 79–98, Cambridge Univ. Press, New York, 1993.

Salisbury, J. W., and J. W. Eastes, The effect of particle size and porosity on spectral contrast in the mid-infrared, *Icarus*, *64*, 586–588, 1985.

Salisbury, J. W., and A. Wald, The role of volume scattering in reducing spectral contrast of reststrahlen bands in spectra of powdered minerals, *Icarus*, *96*, 121–128, 1992.

Salisbury, J. W., and L. S. Walter, Thermal infrared (2.5–13.5 μm) spectroscopic remote sensing of igneous rock types on particulate planetary surfaces, *J. Geophys. Res*, *94*(B7), 9192–9202, 1989.

Salisbury, J. W., B. Hapke, and J. W. Eastes, Usefulness of weak bands in midinfrared remote sensing of particulate planetary surfaces, *J. Geophys. Res.*, *92*, 702–710, 1987a.

Salisbury, J. W., L. S. Walter, and N. Vergo, Mid-infrared (2.1–25 μm) spectra of minerals: First Edition, *U.S. Geol. Surv. Open File Rep.*, 87–263, 1987b.

Salisbury, J. W., D. M. D'Aria, and E. Jarosewich, Mid-infrared (2.5–13.5 μm) reflectance spectra of powdered stony meteorites, *Icarus*, *92*, 280–297, 1991.

Salisbury, J. W., L. S. Walter, N. Vergo, and D. M. D'Aria, *Infrared* (*2.1–25* μm) *Spectra of Minerals*, 267 pp., Johns Hopkins Univ. Press, Baltimore, Md., 1992.

Salisbury, J. W., A. Wald, and D. M. D'Aria, Thermal-infrared remote sensing and Kirchhoff's law: 1. Laboratory measurements, *J. Geophys. Res.*, *99*, 11,897–11,911, 1994.

Schueler, C. F., S. H. Silverman, M. I. Greenfield, and P. R. Christensen, Advanced planetary thermal spectroscopy, in *1997 IEEE Aerospace Conference*, Inst. of Electr. and Electron. Eng., New York, 1997.

Smith, M. D., C. J. Conrath, J. C. Pearl, and E. A. Ustinov, Retrieval of atmospheric temperatures in the Martian planetary boundary layer using upward-looking infrared spectra, *Icarus*, *124*, 586–597, 1996.

Smith, M. D., J. C. Pearl, B. J. Conrath, and P. R. Christensen, Thermal Emission Spectrometer results: Mars atmospheric thermal structure and aerosol distribution, *J. Geophys. Res.*, *106*, 23,929–23,945, 2001a.

Smith, M. D., J. C. Pearl, B. J. Conrath, and P. R. Christensen, One Martian year of atmospheric observations by the Thermal Emission Spectrometer, *Geophys. Res. Lett.*, *28*, 4263–4266, 2001b.

Squyres, S. W., et al., Athena Mars Rover science investigation, *J. Geophys. Res.*, *108*(E12), 8062, doi:10.1029/2003JE002121, in press, 2003.

Thomson, J. L., and J. W. Salisbury, The mid-infrared reflectance of mineral mixtures (7–14 μm), *Remote Sens. Environ.*, *45*, 1–13, 1993.

Van der Marel, H. W., and H. Beeutelspacher, *Atlas of Infrared Spectroscopy of Clay Minerals and Their Admixtures*, 396 pp., Elsevier Sci., New York, 1976.

Vincent, R. K., and G. R. Hunt, Infrared reflectance from mat surfaces, *Appl. Opt.*, *7*, 53–59, 1968.

Vincent, R. K., and F. Thompson, Spectral compositional imaging of silicate rocks, *J. Geophys. Res.*, *17*(14), 2465–2472, 1972.

Wald, A. E., and J. W. Salisbury, Thermal infrared emissivity of powdered quartz, *J. Geophys. Res.*, *100*, 24,665–24,675, 1995.

Wilson, E. B., Jr., J. C. Decius, and P. C. Cross, *Molecular Vibrations: The Theory of Infrared and Raman Vibrational Spectra*, McGraw-Hill, New York, 1955.

Wyatt, M. B., V. E. Hamilton, J. H. Y. McSween, P. R. Christensen, and L. A. Taylor, Analysis of terrestrial and Martian volcanic compositions using thermal emission spectroscopy: 1. Determination of mineralogy, chemistry, and classification strategies, *J. Geophys. Res.*, *106*, 14,711–14,732, 2001.

S. Anwar, G. Cannon, P. R. Christensen, N. Gorelick, R. Kheen, G. L. Mehall, and T. Tourville, Department of Geological Sciences, Arizona State University, Campus Box 876305, Tempe, AZ 85287-6305, USA. (phil.christensen@asu.edu)

D. Bates, S. Ferry, T. Fortuna, J. Jeffryes, W. O'Donnell, R. Peralta, S. H. Silverman, and T. Wolverton, Raytheon Santa Barbara Remote Sensing, 75 Coromar Drive, Goleta, CA 93117, USA.

D. Blaney, R. Denise, and J. Rademacher, Jet Propulsion Laboratory, 4800 Oak Grove Drive, Pasadena, CA 91109, USA.

R. V. Morris, NASA Johnson Space Center, Code SR, Houston, TX 77058, USA.

S. Squyres, Department of Astronomy, Cornell University, 424 Space Sciences Building, Ithaca, NY 14853-6801, USA.